iFlpMosaics enable the multispectral barcoding and high-throughput comparative analysis of mutant and wildtype cells

Irene Garcia-Gonzalez[1], Stefano Gambera[1], Alvaro Regano[1], Susana F. Rocha[1], Lourdes Garcia-Ortega[1], Mariya Lytvyn[1], Luis Diago-Domingo[1], Maria S. Sanchez-Muñoz[1], Aroa Garcia-Cabero[1], Ivana Zagorac[1], Wen Luo[1], Macarena Fernández-Chacón[1], Verónica Casquero-Garcia[1], Federica Francesca Lunella[1], Rui Benedito[1].*

1-Molecular Genetics of Angiogenesis Group, Centro Nacional de Investigaciones Cardiovasculares (CNIC), Madrid, Spain.

* Corresponding author. Rui.Benedito@cnic.es

Abstract

To understand gene function, it is necessary to compare cells carrying the mutated target gene with normal cells. In most biomedical studies, the cells being compared are in different mutant and control animals and therefore do not experience the same epigenetic changes and tissue microenvironment. The experimental induction of genetic mosaics is essential to determine a gene cell-autonomous function and to model the etiology of diseases caused by somatic mutations. Current technologies used to induce genetic mosaics in mice lack either accuracy, throughput or barcoding diversity. Here, we present a large set of new genetic tools and mouse lines that enable Flp recombinase-dependent ratiometric induction and single-cell clonal tracking of multiple fluorescently labeled wildtype and Cre-mutant cells within the same time window and tissue microenvironment. The labeled cells can be profiled by multispectral imaging or by FACS and scRNA-seq. This technology facilitates the induction and analysis of genetic mosaics in any cell type and for any given single or combination of floxed genes. iFlpMosaics enables a more accurate understanding of how induced genetic mutations affect the biology of single cells during tissue development, homeostasis, and disease.

Introduction

The targeted deletion or mutation of a gene triggers a cascade of events in the cell that can significantly alter its phenotype and over time also the surrounding tissue. Scientists often analyze cells or tissues that have carried genetic mutations for several days, weeks, months, or even years and compare their phenotype with that of independent control cells or tissues from distinct non-mutant (control) animals. During the process from gene mutation to phenotypic manifestation and analysis, the biology of the

34 targeted and surrounding tissue often undergoes significant changes that can interact with and alter the
35 final phenotype of the mutant cells. An example of this is the conditional deletion or activation of genes
36 important for vascular, neuronal, or cancer development. Mutations that impact tissue function or
37 development frequently result in changes to the surrounding tissues. Since the non-targeted tissues that
38 surround mutant cells are themselves a source of biochemical factors, any alteration to their
39 development or function will trigger changes in a key tissue feedback mechanism; and any such changes
40 will impact the phenotype of the mutant cells in a non-cell-autonomous manner that is independent of
41 the initially induced genetic mutation itself (Hansen and Hippenmeyer, 2020; Hansen et al., 2022). Over
42 time, this phenomenon often generates secondary mutant tissue phenotypes that can confound
43 interpretation of the primary impact of a gene mutation on a cell's phenotype.

44 Genetic mosaics are a powerful research tool for overcoming these problems because they allow the
45 study of cell-autonomous genetic effects when mutant and control (wildtype) cells arise from the same
46 progenitor cells and confront the same microenvironment in the same tissue or organism. In this
47 scenario, the only difference between the cells being compared is the induced mutation, in an otherwise
48 identical organism, genetic background, and tissue microenvironment.

49 Mouse models that allow the timed induction of somatic genetic mosaics are therefore essential for a
50 comparative analysis of how mutant and control cell phenotypes develop over time in the same
51 microenvironment. Such models also provide the only way to accurately study and model biological
52 processes involving sporadic somatic mutations and their effect on cell proliferation, differentiation, or
53 competition.

54 In *Drosophila*, interchromosomal mitotic recombination associated with distinct tissue markers has
55 been widely used to induce and track genetic mosaics. A similar approach, called MADM (mosaic
56 analysis with double markers), has been developed in mice to allow the labeling of control and mutant
57 cells with different fluorescent markers (Contreras et al., 2021; Zong, 2014; Zong et al., 2005). This
58 method allows full correlation between the expression of a given fluorescent marker and the genetic
59 status (wildtype, heterozygous, or knockout) of the locus carrying the mutation, thus significantly
60 decreasing the rates of false positives and false negatives. However, the method relies on difficult-to-
61 achieve interchromosomal Cre-dependent recombination events, which overall leads to the generation
62 of very few clones of labeled control and mutant cells in a Cre-expressing tissue. Due to the rarity of
63 the interchromosomal recombination events, these genetic mosaics cannot be efficiently induced with
64 tamoxifen-inducible CreERT2 lines, which are weaker and only transiently active. Moreover, this
65 technology cannot be used in quiescent cells and requires chromosomal genetic linkage between the
66 engineered MADM elements and another gene mutation, which significantly complicates the required
67 mouse crosses and genetics, limiting its general applicability. MADM is also incompatible with

68 epistasis analyses that require simultaneous loss-of-function of multiple genes present in distinct
69 chromosomes.

70 Given the complexity and limitations of MADM, the most widely used method for generating
71 conditional somatic genetic-mosaics in the mouse remains the much simpler CreERT2 recombinase-
72 dependent mosaic induction of floxed-gene (flanked by loxP sites) deletion. With this method, the
73 location, timing, and frequency of the recombination events can be regulated by restricting CreERT2
74 expression to a specific tissue and by varying the timing and dose of treatment with the CreERT2
75 activating ligand tamoxifen. This much simpler method requires the use of independent fluorescent
76 reporters of Cre-recombination in order to detect cells with CreERT2 activity. However, several studies
77 have shown that Cre-activity reporter alleles only accurately report recombination of themselves, and
78 cannot be used to reliably report recombination of other floxed genes (Fernandez-Chacon et al., 2019;
79 Liu et al., 2013; Schmidt-Supprian and Rajewsky, 2007). Thus, though much easier to implement than
80 MADM, CreERT2-dependent genetic mosaic approaches generate a high frequency of false positives
81 and false negatives and should not be used for mosaic genetics.

82 To overcome the limitations of current methods for the generation of genetic mosaics in mice, we have
83 developed *iFlpMosaics*, a compendium of new genetic tools and mouse lines that enable FlpO-
84 dependent-induction of multispectral and ratiometric genetic mosaics of both wildtype and mutant cells
85 in the same tissue of an animal. *iFlpMosaics* provide high cellular barcoding and clonal resolution and
86 tighter control of the frequency of genetic mosaicism over time. This technology is also compatible
87 with all existing floxed alleles, and can be induced in any quiescent tissue or progenitor cells. The cell
88 profiling and comparative analysis can be done by *in situ* multispectral imaging, or *ex situ* by FACS or
89 single-cell RNA-seq (scRNAseq). *iFlpMosaics* will enable the accurate and high-throughput
90 quantitative analysis how an individual or combinatorial set of genetic mutations affects the biology of
91 single cells during tissue development, regeneration, or disease.

92

93 **False positives and false negatives with Cre-dependent mosaic genetics**

94 CreERT2 genetics is prone to the induction of false positives and false negatives at high
95 frequency. False positives are cells that recombine/express a reporter while failing to delete the
96 independent floxed target reporter or gene. Conversely, false negatives are cells that delete the target
97 floxed gene but do not recombine the specific reporter allele (Fig. 1a). The high frequency of false
98 positive and false negative cells with CreERT2 genetics has been reported (Fernandez-Chacon *et al.*,
99 2019; Liu *et al.*, 2013), but so far no study has systematically quantified their occurrence for multiple
100 reporter alleles and at the lower induction rates and tamoxifen doses required for mosaic genetics. In
101 order to do this, we analyzed several independent mouse lines containing different Cre-reporters located
102 in the Rosa26 locus, thus allowing us to detect false positives or false negatives among different Cre-

103 reporters by FACS or histology. This analysis showed that different Cre-reporters recombine at
104 significantly different relative frequencies, even when located in the same accessible Rosa26 locus and
105 having similar genetic distances between loxP sites (Fig. 1b). As expected, the chance of finding cells
106 with dual recombination of two reporters (true positives) decreased with decreasing tamoxifen dose and
107 genetic mosaicism (Fig. 1c, 1d). Single-cell functional genetic or clonal analysis usually requires a
108 decrease in the tamoxifen dose in order to ensure sparse labeling of mutant and wildtype cells in the
109 tissue. Unequivocal identification of single cells and their clones over long periods of time requires a
110 recombination rate of 0.01%-10%. We found that at these recombination frequencies the rate of true
111 positives with CreERT2 genetics was very low (Fig. 1c, 1d).

112 These data show that most CreERT2-based *in vivo* functional genetic studies using mosaic
113 genetics or sparse cell labeling will not achieve the desired targeted gene deletion in the labeled cells,
114 and therefore will be unable to uncover the real effect of the targeted gene on single-cell biology with
115 high accuracy and statistical power.

116

117 **Design and validation of *iFlpMosaic* mice**

118 To overcome these problems with CreERT2-dependent mosaic genetic technologies, we
119 developed a toolbox consisting of several mouse lines that allow the FlpO/FlpOERT2-recombinase-
120 dependent induction of ratiometric mosaics of fluorescent mutant cells (gene KO) and normal cells
121 (gene wildtype) (Fig. 1e, 1f and Sup. Fig. 1a, b). We call these new mouse alleles *iFlpMosaics* (R26-
122 $iFlp^{MTomato\text{-}Cre/MYFP}$ and Tg-$iFlp^{MTomato\text{-}H2B\text{-}GFP\text{-}Cre/MYFP\text{-}H2B\text{-}Cherry\text{-}FlpO}$). They contain the ubiquitously
123 expressed CAG promoter and several distinct and mutually exclusive FRT sites (Cai et al., 2013) that
124 enable multispectral labeling and fate-mapping of different mutant cells expressing the fluorescent
125 membrane-tagged tomato protein (MTomato) and Cre, as well as of wildtype cells expressing
126 membrane tagged YFP (MYFP), in any tissue expressing FlpO or FlpOERT2. The two *iFlpMosaic* lines
127 differ either in the genomic location (ROSA26 versus random transgene) or in the expression of
128 additional chromatin-bound fluorescent proteins (H2B-tag) for increased cell resolution and
129 quantitative power (Fig. 1e, 1f and Sup. Fig. 1a, b).

130 Transfection of *iFlpMosaic* ES cells with FlpO-expressing plasmids or induction of these
131 mosaics in mice carrying *FlpO/FlpOERT2* alleles induced the expected ratiometric mosaic of
132 MTomato+ and MYFP+ cells, with very few cells being double positive due to recombination during
133 the G2/M phase of the cycle (Fig. 1e, 1f, and Supplementary Fig. 1c-g). The observed higher frequency
134 of MTomato+ cells is consistent with the shorter genetic distance between the FRTF3 sites than between
135 the FRT5T2 sites (Fig. 1e and Sup. Fig. 1a, b, e). In ES cells and mice, the initially induced cell ratios
136 did not change after prolonged culture or during tissue development *in vivo* (Fig. 1g and Sup. Fig. 1h),
137 showing that expression of MTomato-2A-Cre (or MYFP) is not deleterious to cells. Notably, we found
138 on average 10 times lower expression of the MTomato-2A-Cre cassette in *iFlpMosaic* mice than in the

139 previously generated *iSuRe-Cre* mice (Fig. 1h), further reducing the possibility of Cre-toxicity
140 (Fernandez-Chacon *et al.*, 2019). This difference in expression is due to the different DNA expression
141 elements and genomic location of these alleles.

142 In previous reports, inducible Cre-expressing alleles located in the Rosa26 locus were found to
143 be leaky and to induce germline recombination, even in the absence of FlpO/CreERT2 activity
144 (Fernandez-Chacon *et al.*, 2019; Lao et al., 2012). Given that the *iFlpMosaic* alleles contain Cre- and
145 FlpO-expressing cassettes that can be expressed if the upstream transcriptional stop signals are bypassed
146 (as shown in previous mouse lines), we checked if *iFlpMosaic* mice were also leaky. None of the
147 analysed *iFlpMosaic* mice had leaky expression of the fluorescent proteins contained in their constructs
148 in the absence of an extra allele expressing FlpO (Sup. Fig. 1i). Crosses of *iFlpMosaic* mice with the
149 $Rosa26^{LSL\text{-}YFP}$ Cre-reporter mice revealed a very low percentage of non-self Cre-leakiness in some
150 organs of the $Tg\text{-}iFlp^{Tomato\text{-}H2B\text{-}GFP\text{-}Cre/YFP\text{-}H2B\text{-}Cherry\text{-}FlpO}$ mouse line, but not the R26-$iFlp^{MTomato\text{-}Cre/MYFP}$ line
151 (Sup. Fig. 1i).

152 Significantly more important than false negatives is the occurrence of false positives. In
153 *iFlpMosaic* mice, MTomato-2A-Cre+ cells efficiently recombined other Cre-reporter alleles and all
154 floxed genes tested (Fig. 1i. 1j), ensuring high genetic reliability at single-cell resolution. For example,
155 induction of *iFlpMosaics* in the *Rbpj* floxed background results in only 3.5% Tomato-2A-Cre+ cells in
156 arteries versus 96% in veins and capillaries (Fig. 1k), indicating high gene-deletion efficiency of this
157 master regulator of arterial development. Together, these data show that *iFlpMosaics* provide a very
158 high rate of properly labeled and assigned mutant and wildtype cells. This is in stark contrast to standard
159 CreERT2 mosaic genetics (Fig. 1c, 1d) and similar to the MADM system (Contreras *et al.*, 2021; Zong,
160 2014; Zong *et al.*, 2005). *iFlpMosaic* alleles thus enable the tightly controlled induction of reliable and
161 ratiometric mosaics of mutant and wildtype cells in any tissue expressing FlpO or FlpOERT2;
162 moreover, they provide both membrane and nuclear fluorescent markers for tracking mutant and
163 wildtype cell proliferation, differentiation, or migration at very high resolution (Sup. Fig. 2).
164

165 **Generation of ubiquitous and tissue-specific FlpOERT2 mouse lines**

166 Multispectral genetic mosaics are a particularly valuable research tool if they can be induced at
167 a specific time point and in a significant number of cells, something that is not possible with the MADM
168 system (Contreras *et al.*, 2021; Zong, 2014; Zong *et al.*, 2005). To obtain temporal control over Flp
169 activity or induction, previous studies generated mouse lines that enabled the constitutive (Rosa26) or
170 tissue-specific expression of FlpeERT or the mammalian codon-optimized FlpOERT (Hunter et al.,
171 2005; Kranz et al., 2010). These studies showed that FlpOERT2 activity is significantly lower than
172 CreERT2, and very few cells in each organ were shown to recombine (Lao *et al.*, 2012). In agreement
173 with this, we found that the published $R26^{CAG\text{-}FlpOERT2}$ line recombined the $R26\text{-}iFlp^{MTomato\text{-}Cre/MYFP}$ allele
174 in only ~0.2% of embryonic cells, and was also weak in postnatal and adult organs (Fig. 2a).

175 To enhance FlpOERT2 expression, we therefore sought to develop new constructs containing
176 optimized DNA elements (Cai *et al.*, 2013; Pontes-Quero et al., 2017) (Fig. 2b). We generated and
177 screened 5 transgenic ubiquitous-FlpOERT2 mouse lines with variable copy number (Fig. 2c).
178 Compared with the established *R26*$^{CAG\text{-}FlpOERT2}$ line, the best of these new *Tg(Ins-CAG-FlpOERT2)* lines
179 (here called *Tg(Ins-CAG-FlpOERT2)*$^{\#F2}$) induced several-fold higher recombination of the *iFlpMosaic*
180 allele in embryos and different organs and cell types (Fig. 2d-g and Sup. Fig. 3a-c). With this higher
181 recombination frequency, we frequently observed mutant (MTomato+) and wildtype (MYFP+) cells
182 close to each other, enabling direct comparison of cells experiencing the same tissue microenvironment
183 (Fig. 2f, 2g, Sup. Fig. 3d). As expected, the recombination rate differed between cell types and organs.
184 We confirmed that the ubiquitous and strong *FlpOERT2* expression is not leaky (Sup. Fig. 3e).

185 Besides generating ubiquitous *FlpOERT2* lines of general relevance, we also developed a
186 method to easily target and modify pre-existing and pre-validated *CreERT2*-expressing transgenic
187 alleles to achieve tissue-specific expression of *FlpOERT2*. We designed unique guide RNAs and donor
188 DNAs containing FlpO that allow the efficient conversion of any established *CreERT2* allele into a
189 *FlpOERT2* expressing allele (Fig. 2h). Using this method, we converted an existing PAC *Cdh5-*
190 *CreERT2* mouse line (Wang et al., 2010) containing 4 copies of the *CreERT2* sequence into PAC *Cdh5-*
191 *FlpOERT2* mouse lines containing 3 or 4 copies of the *FlpOERT2* sequence (Fig. 2i). Of the two founder
192 lines obtained, only the *Cdh5-FlpOERT2*^{F1} line had no residual Cre sequence or activity (Fig. 2h). As
193 expected, this line was expressed and induced specific recombination in endothelial cells (ECs, Fig.2j).

194

195 **Ratiometric functional genetics with *iFlpMosaic* mice**

196 Unlike classical Cre-reporters or the *iSuRe-Cre* allele, *iFlpMosaics* are ratiometric by design.
197 This allows quantification by histology or FACS of the relative frequencies of mutant (MTomato-2A-
198 Cre+) and wildtype (MYFP+) cell populations induced in the same tissue and experiencing the same
199 microenvironment throughout the pulse–chase period. We envisioned that this property would allow
200 high-throughput and accurate analysis of the cell-autonomous function of genes in virtually all cell
201 types and over long periods. Such an analysis is not possible with classical Cre/CreERT2 mosaic
202 genetics, because of the high frequency of false positives and negatives (Fig. 1c, 1d) and because Cre-
203 ERT2 genetics does not enable the simultaneous labelling of wildtype cells, which provide an important
204 internal control.

205 To demonstrate the power of *iFlpMosaic* mice to reveal the effect of induced mutations in
206 multiple cell lineages, we intercrossed them with mice containing either the *Tg(ACTFLPe)9205Dym*
207 allele (Rodriguez et al., 2000) (abbreviated here as *ACTB:FlpE*; this allele recombines early embryo
208 progenitor cells*),* the *Apln-FlpO* allele (Luo et al., 2021) (recombines endothelial and derived
209 hematopoietic cells), or the new *Tg(Ins-CAG-FlpOERT2)* allele (induces recombination at any stage

210 and in all cell types). These alleles were further combined with floxed alleles for the *Myc* and *Foxo*
211 genes, which are considered to be important for the proliferation and differentiation of most cell types
212 (Claveria et al., 2013; Eijkelenboom and Burgering, 2013).

213 When the *R26-iFlp*$^{MTomato\text{-}Cre/MYFP}$ allele was combined with the *ACTB:FlpE* or *Apln-FlpO*
214 alleles and the *Myc and Foxo* floxed alleles, mosaic mutant animals survived until adult stages, unlike
215 embryos carrying mutations of these genes in all cells or in all ECs (Dharaneeswaran et al., 2014; He
216 et al., 2008). To understand how these genes affected the biology of different cell types, we first
217 conducted a high-throughput FACS analysis to score the relative ratios of mutant cells (MTomato-Cre+)
218 and wildtype cells (MYFP+) in major organs of postnatal day 7 animals. The assumption was that if the
219 targeted gene is important for a given cell type or organ, its deletion would change the proliferation or
220 differentiation rate of the mutant cells, and this would be noticed in the final MTomato+/MYFP+ log
221 ratio detectable by FACS. This analysis revealed that the impact of MYC loss depended on the cell type
222 and organ. MYC loss has previously been linked to a general competitive disadvantage (Claveria *et al.*,
223 2013) and a lack of proliferation by ECs (Wilhelm et al., 2016). However, we found that mosaic *Myc*
224 deletion had a relatively minor effect on EC clonal expansion throughout embryonic development (Fig.
225 3a). Instead, the highest sensitivity to the mosaic loss of MYC was observed in the hematopoietic
226 lineage (Fig. 3b and Sup. Fig. 4a, b). Unlike liver and lung, heart CD31-CD45- cells were not
227 significantly affected by *Myc* deletion (Fig. 3c), likely due to compensation by the homologous *Mycn*
228 gene in cardiomyocytes as previously reported (Munoz-Martin et al., 2019).

229 We also confirmed the ability of the system to support mosaic epistasis analysis of mutant cells
230 having multiple deleted genes, in this case 3 *Foxo* genes (6 floxed alleles). Foxo genes partially
231 compensate each other's function in several cell types, and together they are considered important
232 negative regulators of cell proliferation and metabolism downstream of AKT signaling, preventing
233 uncontrolled cell growth (Eijkelenboom and Burgering, 2013; Paik et al., 2007; Wilhelm *et al.*, 2016).
234 Surprisingly, our analysis showed that mosaic deletion of three *Foxo* genes (*Foxo1/3/4*^{KO}) had relatively
235 minor consequences for cell expansion in the liver and lung, but especially affected heart cells (Fig.
236 3d). This suggests cell-type and organ-specific functions for *Foxo* genes. The data also show that
237 postnatal retinal ECs are especially responsive to the loss of *Foxo1/3/4*. These cells were much more
238 proliferative, formed dense clusters, and outcompeted wildtype cells over time (Fig. 3e), in line with
239 the vascular phenotypes and hemangiomas shown previously using standard CreERT2 genetics (Paik
240 *et al.*, 2007; Wilhelm *et al.*, 2016).

241 Overall, these results show the utility of *iFlpMosaics* technology for the accurate modeling and
242 high-throughput analysis by FACS or tissue imaging of the impact of somatic mutations on cellular
243 expansion and competition. In this particular case, *iFlpMosaics* analysis revealed that MYC and FOXO

244 proteins are dispensable for the proliferation of many cell types in diverse organs, with MYC being
245 more important in the blood lineage and FOXOs in retina ECs and heart cells.

246

247 **Combining *iFlpMosaic with iFlp*^{Chromatin} for higher single-cell clonal resolution**

248 An important potential application of *iFlpMosaics* technology is the direct live imaging of Cre-mutant
249 and adjacent fluorescent wildtype cells. However, although live microscopy imaging is routine for many
250 species and developmental model systems, it is still not possible or practical for most mouse tissues and
251 laboratories due to the deep tissue location of most cells, the lack of appropriate microscopes, and the relatively
252 slow pace of the biological processes under study. Analysis of how single cells proliferate, differentiate, and
253 migrate in a mouse tissue requires advanced pulse–chase genetic and imaging tools. The *Brainbow* and *Confetti*
254 genetic tools and *Dual ifgMosaics* were generated for this purpose (Livet et al., 2007; Pontes-Quero *et al.*,
255 2017; Snippert et al., 2010). Compared with standard unicolor or single-molecule reporters of Cre activity,
256 multispectral mosaics allow more precise and quantitative single-cell, retrospective, and clonal lineage tracing,
257 due to the lower probability of a cell having a given stochastic recombination event or barcode. To increase the
258 quantitative single-cell resolution of the *iFlpMosaics* technology, we combined the *Rosa26-iFlp*$^{MTomato\text{-}Cre/MYFP}$
259 allele with the published *Rosa26-iChr2-Mosaic* allele (also named here as *iCre*$^{H2B\text{-}Cherry/GFP/Cerulean}$, see Sup. Fig.
260 4c) (Pontes-Quero *et al.*, 2017). This enabled the stochastic and mutually exclusive expression of fluorescent
261 proteins located in nuclei (for cell unit counts) or the cell membrane (for cell shape) in mutant cells (MTomato-
262 2A-Cre+), expanding the diversity of cell barcoding from 1 to 3 possible mutant cells (Fig. 4a).

263 Despite its higher clonal resolution for single MTomato+ mutant cells, this method does not permit
264 quantification of the clonal expansion of single MYFP+ wildtype cells in the same microenvironment and at
265 the same level of resolution. To obtain higher clonal resolution in wildtype cells, we developed the *iFlp*^{Chromatin}
266 mouse line (also called *iFlp*$^{H2B\text{-}Cherry/GFP/Cerulean}$), in which three distinct and incompatible FRT sites enable the
267 generation of a Flp-recombinase-dependent mosaic of cells expressing three distinct chromatin-localized
268 (H2B-tag) fluorescent proteins (Fig. 4b, 4c). When crossed with the *Tg(Ins-CAG-FlpOERT2)* and *iFlp*$^{MTomato\text{-}}$
269 $^{Cre/MYFP}$*-Mosaic* lines, this new *iFlp*^{Chromatin} allele allowed us to generate up to 8 dual-labeled cells (4 mutant
270 and 4 wildtype), significantly increasing the single-cell clonal lineage tracing resolution of mutant and
271 wildtype cells in the same tissue microenvironment (Fig. 4d). These alleles can also be combined with the
272 published Cre-dependent Tg(*iMb2-Mosaic*) allele (or *iCre*$^{MYFP/Tomato/MTFP1}$) (Pontes-Quero *et al.*, 2017) to
273 provide even higher single-cell or clonal resolution of mutant cells (Tomato+ with 12 different fluorescent
274 barcodes) and wildtype cells (YFP+ with 4 different fluorescent barcodes or YFP- with 3 different barcodes)
275 (Fig. 4e). When compared with MADM, this technology provides significantly higher barcoding
276 diversity and clonal resolution of both mutant and wildtype cells, and also allows the labeling and
277 identification of binucleated and polyploid cells, such as adult liver hepatocytes (Fig. 4f).

278

279 **Single-cell functional mosaic genetics with *iFlpMosaics***

280 As an example, we show here how these new mouse alleles and technology enabled us to
281 accurately quantify how single mutant and wildtype cells clonally expand, migrate, and survive when induced
282 at the same time and in the same tissue microenvironment.

283 In the liver, a high percentage of neonatal hepatocytes are in S-phase (EdU+) or in cycle
284 (Ki67+) at P1 and P7, and most stop dividing before P20 (Fig. 5a). However, hepatocyte single-cell
285 clonal expansion dynamics are still unknown. *iFlpMosaic x iFlp*^{Chromatin} mice were induced at P1, and livers
286 were collected at P20 for multispectral imaging and single-cell clonal analysis. Multispectral confocal scanning
287 and spatial mapping of clones revealed that hepatocyte proliferation (clones with 2 cells or more) was dispersed
288 throughout the liver (Fig. 5b and Sup. Fig. 5a,b). The recombination frequency varied among animals, but the
289 average clone size obtained was still similar (Fig. 5c), confirming that there is enough multispectral clonal and
290 quantitative resolution at both low and high *iFlpMosaic* recombination frequencies. These data revealed that
291 17.2% of neonatal hepatocytes did not expand clonally, with most hepatocytes (69%) dividing only once or
292 twice in 20 days. Only 2.4% of single hepatocytes yielded clones with 8 or more cells. The average clone size
293 for wildtype cells was 2.9, in agreement with the observed 2.9-fold liver weight increase from P1 to 20 (Fig.
294 5c, d). Comparison of clonal expansion between wildtype (MYFP+) and mutant *Myc*^{KO} (Mtomato-2A-Cre+)
295 hepatocytes revealed that MYC is necessary for optimal postnatal hepatocyte clonal expansion. Mean *Myc*^{KO}
296 hepatocyte clone size was 2.25, and these clones generated only 125% more hepatocytes (125 new hepatocytes
297 for every 100) over 20 days, whereas wildtype-cell clone size was 2.87, and these clones generated 187% more
298 hepatocytes over the same period (Fig. 5e, f).

299 Single-cell clonal expansion analysis of postnatal pancreatic cells revealed similar Ki67+ and EdU+
300 frequencies to those of liver cells (compare Fig.5a with Sup. Fig. 5c, d). However, *iFlpMosaics* analysis
301 revealed that wildtype pancreatic cells expand significantly more than hepatocytes until P20 (Fig. 5g), with a
302 mean clone size of 3.60 instead of 2.87 (compare wildtype values in Fig. 5h,i with Fig.5e,f). As in the liver,
303 *Myc*^{KO} cells in the pancreas also expanded significantly less than wildtype cells (Fig. 5h, 5i) and were 3.7-fold
304 less frequent than neighboring wildtype cells at the end of the analysis (Fig. 5j).

305 Evidence from recent studies suggested the existence of a highly proliferative hepatocyte population
306 in adult liver, based on a new Dre-inducible Ki67-Cre (ProTracer) allele (He et al., 2021) or CreERT2-based
307 single-cell lineage tracing of a unicolor reporter (Wei et al., 2021). Ki67 immunostaining showed that only
308 1.87% of adult liver hepatocytes are in cycle at any given moment (Sup. Fig.5d). Ki67 can be expressed in
309 metabolically activated (primed and in cycle) or DNA-replicating (S-phase) or in polyploid cells, but many
310 Ki67+ cells will not undergo productive cell division or will die after being in cycle. The *iFlpMosaics* system
311 can measure both productive cell expansion and cell survival. Using the *iFlpMosaic* mice with the highest
312 number of multispectral combinations, and therefore the highest single-cell clonal resolution, we observed very
313 limited proliferation or clonal expansion of single mononucleated or binucleated hepatocytes during the 2

weeks after induction. The mean size of adult hepatocyte clones was 1.10 cells after 2 weeks (Fig. 5k, l), significantly lower than the 1.38 cells after only 1 week of pulsing reported for a simpler unicolor reporter (Wei *et al.*, 2021). During the 2 weeks after induction, only 9.5% of single mononucleated or binucleated diploid hepatocytes underwent productive division or cytokinesis from binucleated cells to form a 2-cell clone (Fig. 5m, n). Proliferation frequency was also low in polyploid hepatocytes (4.9%).

Despite the absence of significant hepatocyte proliferation in homeostasis, when we induced *iFlp* ratiometric mosaics in adult Myc^{flox} livers, we still observed a very significant loss of mutant Myc^{KO} cells (4.2-fold decrease) only 2 weeks after induction (Fig. 5o). Since there is limited clonal expansion of wildtype cells in adult liver (mean clone size 1.10, meaning that only 10 new hepatocytes were generated for every 100 initial hepatocytes over 2 weeks; Fig. 5l), these data suggest that Myc loss induces a significant decrease in adult hepatocyte survival. Interestingly, wildtype hepatocytes expanded more when surrounded by Myc^{KO} hepatocytes than when surrounded by wildtype hepatocytes (compare Fig. 5m/n with 5p/q and Sup. Fig.5e), probably to compensate for the loss of Myc^{KO} hepatocytes. These data suggest the existence of Myc-dependent cell competition among adult hepatocytes, in which cells with lower Myc are less fit and are gradually excluded, as previously shown to occur during early embryonic development (Claveria *et al.*, 2013). This competition and cell turnover may explain why liver cell mass does not increase over time, despite constant cell proliferation. Among the surviving Myc^{KO} mutant cells, we also observed a significant increase in the percentage of binucleated cells and a decrease in the percentage of 2-cell mononucleated clones, suggesting that binucleated Myc^{KO} hepatocytes undergo cytokinesis less frequently than their wildtype counterparts (Sup. Fig. 5e).

iFlp/Dre^{Progenitor} enables induction of genetic mosaics from single progenitor cells

The results above also show that there is significant intercellular clonal variability when different progenitor cells, occupying different tissue locations, are induced. This decreases the statistical robustness of gene-function analysis in single cells and requires a comparative analysis of a large number of single-cell derived clones and averaging of clone-size differences. With the above method, all Tomato+ and all YFP+ clonal populations in a given region can be averaged and compared. However, since the clones derive from different progenitor cells, is not possible to know exactly how loss of a gene changes the cellular and clonal expansion phenotype of a specific single-cell progeny located in a particular niche. The MADM approach allows the generation of labeled wildtype and mutant cells from the same progenitor cell, and in this way gives a very precise estimate of how a gene mutation impacts the mobilization and proliferation phenotypes of a single-cell derived progeny. However, as mentioned above, MADM is a cumbersome method, cannot be effectively induced at a specific time point, and is incompatible with the numerous existing floxed genes.

348 To overcome the limitations of current approaches to understanding the role of genes in single-
349 progenitor cell biology, we designed the *iFlp/Dre*^{Progenitor} DNA construct (Fig. 6a). Injection of this
350 construct into mouse eggs produced four founder transgenic animals, only one of which worked
351 properly and which we called *iFlp/Dre*^{ProgenitorF1}. These *iFlp/Dre*^{Progenitor} alleles can be induced by
352 FlpOERT2 or the stronger DreERT2. Therefore, we also generated a new *Tg(Ins-CAG-DreERT2)*$^{\#F4}$
353 allele by using CRISPR/Cas9 assisted targeting into the pre-existing and screened *Tg(Ins-CAG-*
354 *FlpOERT2)* allele (Fig. 6b). We reasoned that combination of these alleles with *iFlpMosaics* alleles
355 would allow tamoxifen induction of a genetic cascade culminating in the generation of genetic mosaics
356 of mutant and wildtype cells derived from the same progenitor cells. After tamoxifen induction of
357 FlpOERT2 or DreERT2, the *iFlp/Dre*^{Progenitor} allele is recombined, and this triggers the constitutive
358 expression of FlpO, H2B-V5, and the cell-surface marker hCD2. FlpO then effectively recombines the
359 *R26-iFlp*$^{MTomato\text{-}Cre/MYFP}$ allele in H2B-V5+/hCD2+ cells (Fig. 6c). We reasoned that since FlpO is a
360 relatively weak recombinase and full transgene expression takes some time, there would be a
361 corresponding delay in the recombination of the *R26-iFlp*$^{MTomato\text{-}Cre/MYFP}$ allele. During this period, a
362 dividing cell will often generate two or more daughter cells, and in these, the *iFlpMosaic* allele can be
363 recombined in one of two possible ways, generating either Tomato-2A-Cre+ or YFP+ cells in the
364 progeny of a single cell.
365 To test this hypothesis, we injected tamoxifen into P4 mice and collected tissues for analysis 3
366 days later at P7. In animals without the *iFlp/Dre*^{Progenitor} allele, Tomato+ and YFP+ cells arose from
367 independent progenitors that were genetically pulsed in independent locations, and YFP+ wildtype cells
368 were rarely intermixed with mutant Tomato+ cells (Fig. 6d). In animals with the *iFlp/Dre*^{Progenitor} allele,
369 anti-V5 immunostaining enabled the detection of the nuclei of the progenitor cell and its progeny.
370 V5+Tomato+ and V5+YFP+ cells were frequently located close to each other, confirming that they
371 arose from a single progenitor cell (Fig. 6e and Sup. Fig. 6a). This allows for direct comparisons of
372 gene function in the progeny of single progenitor cells.
373 The *iFlp/Dre*^{Progenitor} allele also allowed us to increase the sensitivity to FlpOERT2
374 recombination by 14-fold. With the Cdh5-FlpOERT2 line, we increased EC-recombination efficiency
375 from 3.6% to 51% (Fig. 6f). Recombination efficiency was further increased by combining the
376 *iFlp/Dre*^{Progenitor} allele with *Tg(Ins-CAG-DreERT2)*$^{\#F4}$ instead of *Tg(Ins-CAG-FlpOERT2)*$^{\#F4}$ (Fig. 6g).
377 Another advantage of the *iFlp/Dre*^{Progenitor} allele is the possibility of using anti-hCD2 magnetic
378 beads or antibodies to rapidly isolate the recombined cells, even when they occur at low frequency. The
379 hCD2+ cell population included a 25-fold higher percentage of Tomato+ and YFP+ cells (Fig. 6h),
380 resulting in much faster isolation of these cells, an important consideration when many tissues or
381 infrequent populations need to be isolated on the same day for scRNA-seq analysis.
382
383
384

385 **scRNA-seq of ratiometric *iFlpMosaics* to uncover gene function in all cell types**

386 Recent advances in scRNA-seq methods have allowed unprecedented advances in the understanding
387 of single-cell biology. However, there are three major limitations to the use of scRNA-seq technologies to
388 assess the transcriptome of single mutant and wildtype cells resulting from conditional genetic experiments.
389 The first limitation is the introduction of bias due to the profiling of cells from distinct mutant and wildtype
390 animals that experienced different epigenetic and microenvironmental changes during their lifetime or in
391 disease. The second is the reliance on standard Cre-reporters to define and isolate the mutant cells of interest,
392 since these reporters do not correlate with the desired genetic deletions, particularly in CreERT2-inducible
393 experiments (Fig. 1). The third and most important limitation is uncertainty as to whether the desired floxed
394 gene will be deleted in the pool of analyzed and sequenced mutant single cells. This is important because
395 scRNA-seq technologies only detect the mRNA of some genes in most single cells, and also because
396 many floxed genes conserve their 3´ mRNA sequences after genetic deletion, leading to the
397 transcriptional profile of pseudomutant cells whose true genetic status cannot be accurately determined
398 by standard scRNAseq technologies.

399 Our analysis provides evidence that, unlike other genetic technologies, *iFlpMosaic* alleles allow
400 the reliable isolation of *bona fide* mutant cells and wildtype cells from the same tissue (Fig. 1 and 2).
401 Therefore, we combined *iFlpMosaics* with scRNA-seq to achieve high-throughput scoring of gene
402 function in the proliferation and differentiation of all early embryo cell types. For this analysis, we
403 selected to induce the deletion of *Rbpj*, which encodes a transcription factor essential for Notch
404 signaling, one of the most important pathways for cell proliferation and differentiation during
405 embryonic development (Siebel and Lendahl, 2017). We pulsed embryos with 4-OHT at embryonic
406 day 9.5 (E9.5) and collected Tomato+ (mutant) and YFP+ (wildtype) cells by FACS at E13.5 (Fig. 7a).
407 Based on their transcriptome and known marker genes, we identified 16 major cell types (Fig. 7b). In
408 Tomato-2A-Cre+ cells, deletion of *Rbpj* exons 6 and 7 generates a less stable but still detectable
409 3´mRNA (Fernandez-Chacon et al., 2023), together with a decrease in the expression of the main
410 canonical downstream target *Hes1* (Fig. 7c). The canonical *Hes1* target gene can also be regulated by
411 other pathways. Deletion of *Rbpj* led to changes in the frequency of cells in S-phase (Ki67+ mRNA) in
412 some clusters (Fig. 7c). Global *iFlpMosaic*-driven *Rbpj* deletion at E9.5 compromised the
413 differentiation and expansion of peripheral neurons, ECs, cardiomyocytes, erythrocytes, hepatocytes,
414 and myocytes, whereas the frequency of epithelial and mesenchymal cells increased (Fig. 7d-e). *Rbpj*
415 deletion led to a 5-fold decrease in the frequency of ECs (Fig.7d, e), loss of expression of the arterial
416 marker genes *Gja5* and *Gja4*, and upregulation of the tip-cell genes *Esm1, Kcne3, Apln*, and *Cdkn1a*
417 (Fig.7g,h). This correlates with the essential role of *Rbpj* in the specification of arterial ECs and the
418 inhibition of tip ECs (Luo *et al.*, 2021; Pontes-Quero et al., 2019). $Rbpj^{KO}$ ECs also upregulated genes
419 related to epithelial-to-mesenchymal transition, glycolysis, and angiogenesis and were less frequently
420 in cycle (Fig.7i). scRNAseq data from other cell types revealed that *Rbpj* loss changes the relative

421 frequency of specific cell-type clusters, suggesting an impact on their proliferation or differentiation.
422 Indeed, *Rbpj* deletion dysregulated multiple genes and genetic pathways in the many cell types and
423 clusters identified (Fig. 7j-r and Sup. Fig. 7). These scRNA-seq data provide an important resource for
424 further exploration of the role of Rbpj–Notch signaling in the early expansion and differentiation of
425 embryonic lineages. This analysis also exemplifies how the combination of ratiometric *iFlpMosaics*
426 with scRNA-seq analysis is a very powerful tool for the high-throughput determination of cell-
427 autonomous gene function in all cell types during development or disease.

428

429 **Discussion**

430 Genetic mosaics are essential tools for determining the cell-autonomous function of a gene and avoid
431 the confounding effects frequently associated with classical whole- animal or tissue-specific conditional
432 genetics. With inducible mosaic genetics, the mutant and wildtype cells share the same
433 microenvironment and developmental or physiological history, with the only difference between them
434 being the deleted gene. This provides a much more accurate way to study and understand cell-
435 autonomous gene function during tissue development, homeostasis, or disease.

436 We and others have observed that the transcriptional programs and phenotypes of single mutant cells
437 in genetic mosaics often differ significantly from those of single cells extracted from a tissue in which
438 the same gene was deleted in most cells (Hansen *et al.*, 2022). Comparative omics of mutant and
439 wildtype cells in genetic mosaics will more accurately reveal the true molecular and cellular gene cell-
440 autonomous function. With classical genetics, changes to the mutant tissue function and
441 microenvironment can always impact the transcriptional program of the mutant cells in ways unrelated
442 to the original gene function or genetic program. For example, if a gene mutation impairs vascular
443 development or permeability, this will affect the growth, function, and paracrine signaling of the
444 surrounding tissue, and these effects will in turn influence the mutant-cell phenotype. With inducible
445 genetic mosaics these effects are controlled for, because the wildtype and mutant cells share the same
446 tissue history and microenvironment.

447 Nevertheless, there are several difficulties with the methods most frequently used for mosaic conditional
448 genetics in mice, the most widely used animal model in biomedical research. Genetic mosaics induced
449 by CreERT2 are easy to achieve, but are unreliable (Fernandez-Chacon *et al.*, 2019; Liu *et al.*, 2013;
450 Schmidt-Supprian and Rajewsky, 2007). These models also lack the co-induction of wildtype-cell
451 labeling required for direct phenotypic comparison with mutant and wildtype cells in the same tissue.
452 MADM is genetically very reliable, and provides an internal wildtype cell control, but is a technically
453 cumbersome method that provides no temporal resolution in the induction and genetic analysis
454 (Contreras *et al.*, 2021; Zong, 2014; Zong *et al.*, 2005).

455 The set of new genetic tools we describe here significantly improves on both of these older technologies.
456 Unlike Cre-ERT2 genetics, *iFlpMosaics* provide clearly distinguishable and reliable fluorescent labels
457 for both true mutant cells (Tomato) and true wildtype cells (YFP). The simultaneous and ratiometric
458 induction of fluorescent labels in mutant and wildtype cells in the same tissue is an important feature
459 that allows accurate measurement and comparison of the proliferation, differentiation, migration, and
460 survival of these populations over time. We have shown that this ratiometric analysis is robust over
461 short and long periods of time. The fluorescent markers are easily detectable and quantifiable by
462 microscopic imaging or FACS. Unlike MADM, *iFlpMosaics* provide a high degree of inducibility at
463 any specific time point and in any cell type, including quiescent cells present in adult mice, which will
464 be very important for modeling the etiology of diseases caused by sporadic somatic mutations in
465 quiescent cells, or the consequences of CRISPR-based gene targeting and editing, which are by their
466 nature also mosaic. In addition, *iFlpMosaics* are compatible with all existing floxed mouse alleles,
467 enabling mosaic deletion of one or multiple floxed genes in cis, which is essential to perform functional
468 genetic epistasis with single cell resolution. With *iFlpMosaics,* instead of only 1 cell barcode (as in
469 standard CreERT2 or MADM)*,* up to 12 different multispectral barcodes are possible for mutant cells
470 and up to 7 for wildtype cells. This significantly higher spectral barcode diversity and dual labeling
471 (membrane and nuclei) further increases single-cell and clonal quantitative resolution during a pulse–
472 chase genetic experiment.

473 These new genetic tools allowed us to significantly extend and refine previous findings on the roles of
474 several genes (*Myc*, *Foxo1/3/4* and *Rbpj*) in the development and differentiation of most embryonic
475 lineages, the single cell clonal expansion of postnatal tissues, or the competitive survival of cells during
476 the normal homeostasis and turnover of adult tissues. The ability to induce ratiometric genetic mosaics
477 in multiple cell types at the same time, and at both low and high frequencies, increases the ease and
478 throughput of a gene cell-autonomous function analysis. With *iFlpMosaics*, determining a gene cell-
479 autonomous function no longer requires the crossing of mice carrying the floxed gene with multiple
480 independent CreERT2 lines (one for each cell type).

481 In *iFlpMosaics,* cells expressing MTomato also express Cre, a recombinase that is toxic when expressed
482 at high levels (Loonstra et al., 2001; Naiche and Papaioannou, 2007; Rashbrook et al., 2022). However,
483 we found that the expression of the *iFlpMosaic* alleles is relatively low in comparison with previously
484 published Cre-expressing lines (Fernandez-Chacon *et al.*, 2019). This could be due to the different DNA
485 elements used and the presence of only one upstream insulator during Rosa26 targeting. The PGK-Neo
486 cassette and the 2A peptide elements used in i*FlpMosaic* alleles have been shown to reduce expression
487 or translation efficiency (Ema et al., 2006; Pontes-Quero *et al.*, 2017; Sharma et al., 2012). The absence
488 of Cre toxicity with *iFlpMosaics* was confirmed by the long-term analysis of the Tomato-2A-
489 Cre+:YFP+ cell ratio *in vitro* and *in vivo*. This ratio remained constant over time on a wildtype genetic

490 background, assuring the absence of deleterious effects caused by the permanent Cre expression, similar
491 to what has been shown for hundreds of other existing Cre lines.

492 Single-cell biology during tissue development is highly heterogenous, and it is therefore important to
493 be able to reliably induce and analyze genetic mosaics of mutant and wildtype cells derived from single
494 progenitor cells and with a negligible level of false positives and false negatives. The established
495 MADM technology is ideal for this (Contreras *et al.*, 2021; Zong, 2014; Zong *et al.*, 2005) but lacks
496 temporal inducibility. With the new *iFlp/Dre*^{Progenitor} allele, we were able to significantly increase the
497 inducibility and precision of *iFlpMosaics*. The dual *iFlp/Dre*^{Progenitor} allele is much more sensitive to
498 both FlpOERT2/DreERT2 activity and results in a genetic cascade that includes a delay in the
499 expression of FlpO. This delay is very convenient for generating different mutant and wildtype cells
500 within the progeny of a single progenitor cell, something previously achievable only with MADM. The
501 progeny cells will also permanently express the nuclear marker H2B-V5 and the surface marker hCD2,
502 ideal for FACS or rapid magnetic cell isolation of both mutant and wildtype cells.

503 Establishing the biology of single-cell lineages with high detail and in a realiable and high-throughput manner
504 will require integration of information derived from *in situ* single-cell lineage-tracing microscopy with
505 information derived from new scOMICs and bioinformatic analysis methods. Our analysis shows how the
506 combination of *iFlpMosaics* with FACS or scRNA-seq easily achieves high-throughput analysis of the
507 cell-autonomous function of any gene in all cell types during development, homeostasis, or disease.
508 Since mutant and wildtype cell mosaics can be induced in fewer than 5% of the animal's cells, they will
509 not severely affect tissue or organ development and homeostasis, allowing analysis of the
510 transcriptional, epigenetic, proliferative, and differentiation state of all different types of mutant cells
511 in a mostly wildtype environment. This means that determining cell-autonomous gene function no
512 longer requires crosses of mice carrying the floxed gene with multiple independent CreERT2 lines (one
513 for each cell type). The ubiquituous and strongly expressed FlpOERT2 and DreERT2 lines generated
514 here allow induction of *iFlpMosaics* in all cell types at both low and high frequency respectively. This
515 enables direct comparison of the molecular and cellular phenotypes of mutant and wildtype cells
516 extracted from all tissues within the same embryo or animal.

517 *iFlpMosaics* will greatly facilitate the induction and high-throughput functional analysis of somatic
518 mutations or genetic mosaics. This will be central to understanding how an individual or combinatorial
519 set of genetic mutations affects the biology of single cells during tissue development, regeneration, or
520 disease.
521
522
523
524
525

Methods

Mice

We generated and used Mus musculus lines on the C57BL6 or C57BL6×129SV, or B6CBAF1 genetic backgrounds. All mice were backcrossed to C57Bl6 for several generations. To generate mice for analysis, we intercrossed mice aged between 7 and 30 weeks. We do not anticipate any influence on our data of mouse sex. The following mouse lines were used and intercrossed: *Tg(Cdh5-CreERT2)* (Wang *et al.*, 2010), *Tg(iSuRe-Cre)* (Fernandez-Chacon *et al.*, 2019), *Notch1*$^{flox/flox}$ (Radtke et al., 1999), *Rbpj*$^{flox/flox}$ (Han et al., 2002), *Myc*$^{flox/flox}$ (de Alboran et al., 2001), *Mycn*$^{flox/flox}$ (Knoepfler et al., 2002), *Foxo1/3/4*$^{flox/flox}$ (Paik *et al.*, 2007), *Rosa26-EYFP* (Srinivas et al., 2001), *Rosa26-iChr2-Mosaic* (Pontes-Quero *et al.*, 2017), Tg-*iMb2-Mosaic* or *iCre*$^{MYFP/Tomato/MTFP1}$ (Pontes-Quero *et al.*, 2017), *Gt(Rosa)26*$^{tm3(CAG-FlpOERT2)Ali}$ (Lao *et al.*, 2012), *Gt(Rosa)26Sor*$^{tm14(CAG-LSL-tdTomato)Hze}$ (Madisen et al., 2010), and *Apln-FlpO* (Luo et al., 2021). The following mouse lines were produced in this study: *R26-iFlp*$^{MTomato-Cre/MYFP}$, *Tg-iFlp*$^{MTomato-H2B-GFP-Cre/MYFP-H2B-Cherry-FlpO}$, *Tg(INS-CAG-FlpOERT2)*, *Tg(INS-CAG-DreERT2)*, *Tg(Cdh5-FlpOERT2)*, *iFlp*^{Chromatin}*-Mosaic*, and *Tg-iFlp/Dre*^{Progenitor}.

The *Tg-iFlp*$^{MTomato-H2B-GFP-Cre/MYFP-H2B-Cherry-FlpO}$, *Tg(INS-CAG-FlpOERT2)*, *TgiFlp*^{Chromatin}*-Mosaic*, and *Tg-iFlp/Dre-Progenitor* mouse alleles were generated by standard DNA injection into mouse eggs and screening of several transgenic founders, as indicated in the main text or figures. The *R26-iFlp*$^{MTomato-Cre/MYFP}$ allele was generated by CRISPR-assisted gene targeting of the Rosa26 locus in G4 ES cells, using the guide GACTGGAGTTGCAGATCACGA_GGG (IdT DNA) and a donor DNA with the elements indicated in Figure 1. Targeted ES cells were used for mice production. The *Tg(Cdh5-FlpOERT2)* line was generated by CRISPR-Cas9-assisted gene targeting of the existing *Tg(Cdh5-CreERT2)* line (Wang et al., 2010) in mouse eggs, using the guide AAGCTTATCGATACCGTCGA_CGG and a donor DNA containing the Cdh5-FlpOERT2 sequence. *Tg(INS-CAG-DreERT2)* mice were generated by CRISPR-Cas9 using guide RNAs (GATGTCGAACTGGCTCATGG_TGG and AACAGGCGGATCTGCGTACG_CGG) targeting the existing FlpO sequence contained in the pre-screened *Tg(INS-CAG-FlpOERT2)* transgene and a donor DNA containing the *CAG-DreERT2* sequence. Injection mixtures consisted of 0.305 mM of the described crRNAs (IDT) and tracrRNA (IDT, catalog 1072533) and 20 ng/µL Cas9 nuclease (Alt-R® S.p. HiFi Cas9 Nuclease V3, 100 µg, Catalog 1081060). Founders were initially screened by PCR with the primers described in Supplementary Table 1.

To induce CreERT2, FlpOERT2, or DreERT2 activity in adult mice, 1g tamoxifen (Sigma-Aldrich, P5648_1G) was dissolved in 50 mL corn oil (stock tamoxifen concentration, 20 mg/mL), and aliquots were stored at -20C. Animals received intraperitoneal injections of 50 µL to 150 µL of this stock solution (total dose, 1-to-3 mg tamoxifen per animal at 40-to-120 mg/kg), as indicated in the figures.

561 For treatment of pregnant females, the tamoxifen was dissolved together with progesterone to reduce
562 miscarriage (2mg tamoxifen and 1mg progesterone per mouse). To activate recombination in pups, 4-
563 Hydroxytamoxifen (4-OHT) was injected at the indicated stages at a dose of 40 mg/kg or 4mg/kg body
564 weight, as indicated in the figures. All mouse lines and primer sequences required for genotyping are
565 provided in Supplementary Table 1.

566 All mouse husbandry and experimentation were conducted using protocols approved by local animal
567 ethics committees and authorities (Comunidad Autónoma de Madrid and Universidad Autónoma de
568 Madrid CAM-PROEX 177/14, CAM-PROEX 167/17, CAM-PROEX 164.8/20 and PROEX 293.1/22).
569 The mouse colonies were maintained in racked individual ventilation cages according to current
570 national legislation. Mice had dust and pathogen-free bedding and sufficient nesting and environmental
571 enrichment material for the development of species-specific behavior. All mice had ad libitum access
572 to food and water in environmental conditions of 45%–65% relative humidity, temperatures of 21–
573 24°C, and a 12 h/12 h light/dark cycle. To preserve animal welfare, mouse health was monitored with
574 an animal health surveillance program that followed FELASA recommendations for specific pathogen-
575 free facilities.

576

577 **Immunofluorescence on cryosections**

578 For multispectral *iFlpMosaics* tissue harvesting, mice were euthanized in CO_2 chambers, 10 mL of 50
579 mM KCl were injected into the left ventricles, and whole mice were perfused with 3.7%-4%
580 formaldehyde (ITW Reagents, 252931), at pH 7. Explanted tissues were post-fixed for 2 h in 4%
581 paraformaldehyde (PFA) (Thermoscientific, 043368.9M) in phosphate-buffered saline (PBS) at 4°C
582 with gentle rotation. After three washes in PBS for 10 min each, organs were stored overnight in 30%
583 sucrose (Sigma) in PBS. Organs were then embedded in OCT™ (Sakura) and frozen at –80°C.
584 Cryosections (35 µm) were cut on a cryostat (Leica), washed three times for 10 min each in PBS, and
585 blocked and permeabilized in PBS containing 10% donkey serum (Millipore), 10% fetal bovine serum
586 (FBS), and 1% Triton X-100. Primary antibodies were diluted in the same buffer and incubated with
587 sections overnight at 4°C. This step was followed by three 10 min washes in PBS and incubation for 2
588 h with conjugated secondary antibodies (1:200, Jackson Laboratories) and DAPI in PBS at room
589 temperature. After three washes in PBS, sections were mounted with Fluoromount-G
590 (SouthernBiotech). All antibodies used are listed in Supplementary Table 2.

591

592 **Wholemount immunofluorescence of retinas**

593 For postnatal mouse retina immunostaining, eyes were collected and fixed in ice-cold 4% PFA in PBS
594 for 10 minutes. Eyes were then incubated n the same solution for a further 15 min at room temperature,
595 washed once in PBS, and kept on ice. After microdissection with spring scissors (FST), retinas were
596 fixed in 4% PFA for an additional 45 min at room temperature, followed by two PBS washes of 10 min
597 each. Retinas were blocked and permeabilized for 1 h in PBTS buffer (0.3% Triton X-100, 3% FBS,
598 and 3% donkey serum). Samples were then incubated overnight at 4°C with biotinylated isolectinB4
599 (Vector Labs, B-1205, diluted 1:50) and primary antibodies (Supplementary Table 2) diluted in PBTS
600 buffer. After five washes (20 min each) in PBTS buffer diluted 1:2, samples were incubated for 2 h at
601 room temperature with Alexa-conjugated secondary antibodies (Supplementary Table 2). After three
602 washes of 30 min each in PBTS buffer (diluted 1:2) and two washes of 15 min each in PBS, retinas
603 were mounted with Fluoromount-G (SouthernBiotech).
604

605 **In vivo EdU labeling and detection of EC proliferation**

606 To detect EC proliferation in postnatal liver and pancreas, 20 µg/g body weight EdU (Invitrogen,
607 A10044) was injected intraperitoneally into P1, P7, or P20 mice 4 h before dissection. Livers and
608 pancreases were fixed in 4% PFA and processed for cryosectioning as described above. EdU signals
609 were detected with the Click-it EdU Alexa Fluor 647 or 488 Imaging Kit (Invitrogen, C10340 or
610 C10337). In brief, after all other primary and secondary antibody incubations, samples were washed
611 according to the immunofluorescence staining procedure and then incubated with Click-iT EdU reaction
612 cocktail for 40 min, followed by DAPI counterstaining.

613 **Image acquisition and analysis**

614 For confocal scanning, immunostained organ sections or whole-mount retinas were imaged at high
615 resolution with a SP8 Navigator confocal microscope fitted with a 10x, 20x, or 40x objective. Individual
616 fields or tiles of large areas were acquired. All images shown are representative of the results obtained
617 for each group and experiment. Animals were dissected and processed under exactly the same
618 conditions. Comparisons of phenotypes or signal intensities were made using images obtained with the
619 same laser excitation and confocal scanner detection settings. Fiji/ImageJ was used to threshold, select,
620 and quantify objects in confocal micrographs. Manual and automatic ImageJ public plugins and
621 customed Fiji macros were used for quantification.

622 **Fluorescence activated flow cytometry and sorting**

623 Embryonic, postnatal, or adult tissues were dissociated before fluorescence activated flow cytometry
624 or sorting (FC or FACS). Embryonic tissues were dissociated using the Miltenyi Biotec Tissue
625 Dissociation Kit 2 (130-110-203). Postnatal and adult mouse tissues were first digested for 20min at

626 37ºC with 2.5 mg/mL collagenase type I (Thermofisher), 2.5 mg/mL dispase II (Thermofisher), and
627 50 µg/mL DNAseI (Roche).

628 Dissociated samples were filtered through a 70-µm cell strainer, and cells were centrifuged (400g,
629 4°C for 5 min). Cell pellets were gently resuspended in blood lysis buffer (0.15 M NH_4Cl, 0.01M
630 $KHCO_3$, and 0.01 M EDTA in distilled water) and incubated for 10 minutes on ice to remove
631 erythroid cells. Cells were centrifuged (400g at, 4°C for 5 min), and cell pellets were gently
632 resuspended in blocking solution (PBS without Ca^{2+} or Mg^{2+} and containing 3% dialyzed FBS
633 (Termofisher)) and incubated at 4ºC with shaking for 20min. Cells were centrifuged (300g at 4°C for
634 5 min), resuspended, and incubated for 30min at 4ºC with APC rat-anti-mouse CD31 and APC-CY7
635 anti-CD45 (Supplementary table 2). Cells were then centrifuged (400g, 4°C for 5 min), resuspended,
636 washed in PBS without Ca^{2+} or Mg^{2+}, and centrifuged again, and cell pellets were resuspended in
637 blocking solution. Cells were kept on ice until used for FC or FACS. DAPI (5 mg/mL) was added to
638 the cells immediately before analysis. Cells were routinely analyzed with a LSRFortessa cell analyser
639 or sorted in a FACS Aria Cell Sorter (BD Biosciences). BD FACS Diva V8.0.1 and Flow JO v10
640 were utilized for FACS data collection and analysis.

641

642 **Cell isolation for transcriptomic analysis**

643 For quantitative real time PCR (qRT-PCR) analysis, approximately 20,000 DAPI-negative Tomato+ or
644 YFP+ cells from dissociated tissues were sorted directly to RLT buffer (RNAeasy Micro kit - Qiagen),
645 and RNA was extracted according to the manufacturer's instructions and stored at –80°C. This RNA
646 was later used for qRT-PCR or RNAseq analysis. For qRT-PCR, total RNA was retrotranscribed with
647 the High Capacity cDNA Reverse Transcription Kit with RNase Inhibitor (Thermo fisher, 4368814).
648 cDNA was preamplified with Taqman PreAmp Master Mix containing a Taqman Assay-based pre-
649 amplification pool composed of a mix of the Taqman assays indicated in Supplementary Table 3.
650 Preamplified cDNA was used for qRT-PCR using the same gene-specific Taqman Assays and Taqman
651 Universal Master Mix in an AB7900 thermocycler (Applied Biosystems). Data were retrieved and
652 analyzed with AB7900 software.

653 For RNA-seq analysis, embryos were dissociated using Miltenyi Biotec Tissue Dissociation Kit 2 (130-
654 110-203). A 1.2 mL volume of dissociation solution was placed together with a single embryo in a 2
655 mL round bottom tube. Following a 5-min incubation in a 37°C water bath, tubes were placed inside a
656 pre-warmed 50 mL falcon tube and incubated for 25 min on a MACSmix Tube Rotor. Cells were then
657 resuspended with 30 strokes with a Gilson P1000 pipette, starting slow and increasing speed gradually.
658 To the 1.2 mL cell suspension were added 3 mL of sorting buffer (10% FBS in Ca_2- and Mg_2-free PBS),
659 and the resulting solution was transferred to a 5 mL syringe. This volume was pressed slowly through
660 a small 70 µm strainer to remove clumps. Each embryo yielded around 30 million cells at this stage.

661 Cell suspensions were spun at 400g for 6 minutes, and pellets were detached and resuspended in 300
662 µL sorting buffer containing DAPI. DAPI-negative, single, and live Tomato+ and YFP+ cells were
663 sorted to eppendorf tubes containing 300ul of sorting buffer. Cells (66k Tomato+ and 30k YFP+) were
664 sorted using a 100 µm nozzle, 20 PSI and high purity scale and low flow rate (1) to preserve cell viability
665 and decrease contamination. Sorted cells were spun at 500g for 5min and resuspended in 30-40 µL cell-
666 capture buffer (Ca_2- and Mg_2-free PBS supplemented with 0.04% BSA). After counting cells in
667 Countess 3 Automated Cell Counter (Thermo Fisher Scientific), two independent 10x genomics ports
668 were loaded with either 16k Tomato+ cells (90% viability) or 16k YFP+ cells (88% viability).

669

670 **Next generation sequencing sample and library preparation**

671 Next Generation Sequencing (NGS) experiments were performed in the CNIC Genomics Unit. For
672 scRNA-seq experiments, single cells were encapsulated in emulsion droplets using the Chromium
673 Controller instrument (10x Genomics). scRNA-seq libraries were prepared according to the
674 manufacturer's instructions. The aimed target cell recovery for each port was 10000 cells. Generated
675 libraries were sequenced in a HiSeq4000 or NextSeq2000 system (Illumina).

676

677 **Transcriptomic data analysis**

678 Transcriptomic data were analyzed by the CNIC Bioinformatics Unit, Alvaro Regano, and Irene Garcia.

679 The following pipeline was followed for scRNA-seq data processing and *in silico* cell-type selection.
680 For alignment and quantification of gene expression, the reference transcriptome was built using mouse
681 genome GRCm39 and Ensembl gene build v109 (https://ftp.ensembl.org/pub/release-
682 109/fasta/mus_musculus). The WPRE-sv40pa sequences expressed in the Tomato+ and YFP+ samples
683 were added to the reference. Gene metadata were obtained from the corresponding Ensembl BioMart
684 archive. Reads from transcripts were processed, aligned, and quantified using the Cell Ranger v6.1.2
685 pipeline. Single-cell analysis was based on the Seurat (Hao et al., 2021) and DoubletFinder R packages.
686 Low-quality cells were filtered out using the following criteria: total counts, >1000 and <55,000; genes
687 detected, >500 and <7500; mitochondrial transcripts content, <15%; hemoglobin transcripts, <1%;
688 ribosomal transcripts, <35. Counts were log-normalized and scaled, followed by principal component
689 analysis (PCA) and clustering using the shared nearest-neighbors algorithm and Louvain clustering
690 (settings as defaults except for the 2000 most variable genes, 24 principal components, and a resolution
691 of 0.35). Clusters and cells were classified based on the SingleR method (Aran et al., 2019) using
692 Blueprint ENCODE, the Human Primary Cell Atlas cell-type profile collection, and a scRNASeq mouse
693 dataset from the celldex package. This identification was used to predefine the different cell types
694 present in the dataset for the analysis. Doublets were removed using DoubletFinder, using a first
695 annotation with 24 PCs, 0.25 pN, and a pK of 0.05 and the second annotation with 10 PCs, pN0.25, and

696 pK 0.05. Cells classified as Singlets were preserved. Singlets were then reclustered using 19 PCAs and
697 a clustering resolution of 0.35. Manual curation of the identified clusters was applied to confirm and
698 finetune the identity of the clusters based on the scRNAseq bibliography.

699 **Copy number assay and qRT-PCR**

700 To determine the copy number of *FlpO*- or *Cre*-expressing cassettes after transgenesis, genomic DNA
701 was extracted from mouse tail biopsies. Briefly, blood samples were digested overnight in 500 µL
702 proteinase K solution (10 mM Tris-HCl [pH 8.0], 100 mM NaCl, 10 mM EDTA [pH 8.0], 0.5% sodium
703 dodecyl sulfate, 0.25 mg/mL proteinase K) with occasional vortexing. To this solution were added 250
704 µL each of phenol and chloroform, followed by vigorous vortexing to ensure thorough mixing. Samples
705 were immediately microcentrifuged at maximum speed for 5 minutes to separate the aqueous and
706 organic layers. The upper aqueous layer (300 µL) was removed, with special care taken not to disturb
707 the interface. To 300µl solution were added 30µL (0.1 x volume) of 3M NaAc and 825 µL (2.5 x
708 volume) of 100% EtOH. The tubes were then shaken 10 times to precipitate the DNA. Samples were
709 spun down at maximum speed for at least 45 minutes at 4ºC. The supernatant was removed and pelleted
710 DNA was washed with 500 µL 70% ethanol, followed by centrifuging at max speed for 5 minutes. The
711 washed pellets were resuspended overnight in 100 µL TE solution (Tris 10mM and 0.1mM EDTA, pH
712 8). The next day, DNA concentrations were measured in a NanoDrop microvolume spectrophotometer
713 (Thermo Fisher Scientific) and diluted to a final concentration of 10 ng/µL.

714 For the copy number assays, we performed qRT-PCR with TaqMan Universal Master Mix (TaqMan,
715 4440049) and the following probes: Tert TaqMan Copy Number Reference Assay (TaqMan probe,
716 4458369); a probe and primer set designed in the lab and synthetized by iDT to detect *FlpO* (qPCR
717 FlpO probe: TCTTGATGTCGCTGAACCTGCCG [fluorophore FAM], FlpO-qPCR-F:
718 CTGTACCAGTTCCTGTTCCTG, FlpO-qPCR-R: CTTGTCTTGGTCTCGGTCAC); and a pre-
719 designed Cre assay to detect the *Cre* gene (Mr00635245_cn , ThermoFisher).

720 The relative number of copies of the genes of interest was determined using the Tert probe as a
721 reference. Tert and FlpO/Cre probes were combined in the same reaction since they emit different
722 fluorophores, FAM and VIC. qRT-PCR reactions were run in an AB7900 thermocycler (Applied
723 Biosystems).

724

725 **Statistical analysis and reproducibility**

726 All bar graphs show mean ± s.d. Experiments were repeated with independent animals. Comparisons
727 between two sample groups with a Gaussian distribution were by unpaired two-tailed Student *t*-test.
728 Comparisons among more than two groups were by one-way ANOVA followed by multiple comparison
729 tests. All calculations were done in Excel, and final datapoints were analyzed and plotted with GraphPad

730 Prism. No randomization or blinding was used, and animals or tissues were selected for analysis based
731 on their genotype, the detected Cre/FlpO/Dre-dependent recombination frequency, and the quality of
732 multiplex immunostaining. Sample sizes were chosen according to the observed statistical variation and
733 published protocols.

734

735 **Data availability**

736 RNA-seq data can be viewed at the Gene Expression Omnibus (GEO) under accession number
737 GSEXXXX. Instructions and code to reproduce all scRNA-seq results can be found at
738 https://github.com/RuiBenedito/Benedito_Lab. Unprocessed original photos of the data are available
739 upon request. All other data supporting the findings in this study are included in the main article and
740 associated files.

741 **Acknowledgments**

742 Research in the Benedito laboratory was supported by European Research Council (ERC) Starting Grant
743 AngioGenesHD (638028) and Consolidator Grant AngioUnrestUHD (101001814), the Ministerio de
744 Ciencia e Innovación (SAF2017-89299-P and PID2020-120252RB-I00), and "la Caixa" Banking
745 Foundation (project code HR19-00120 and HR22-00316 AngioHeart). The CNIC is supported by the
746 Instituto de Salud Carlos III (ISCIII), the Ministerio de Ciencia e Innovación (MCIN), and the Pro CNIC
747 Foundation and is a Severo Ochoa Center of Excellence (grant CEX2020-001041-S funded by
748 MICIN/AEI/10.13039/501100011033).

749 Microscopy experiments were performed in the CNIC Microscopy and Dynamic Image Unit, an ICTS-
750 ReDib co-funded by MCIN (/AEI /10.13039/501100011033) and the EDRF "A way to build Europe"
751 (#ICTS-2018-04-CNIC-16).

752 I.G.-G. was supported by a PhD fellowship from Fundación La Caixa (CX-SO-16-1). A.R. was supported
753 by The Youth Employment Initiative (YEI) PEJD-2019-PRE/BMD-16990. L.G.-O. was supported by the
754 Spanish Ministry of Economy and Competitiveness (PRE2018-085283). S. G. was supported by a Juan
755 de la Cierva Fellowship (FJC2020-044237-I). M.F.-C. was supported by PhD fellowships from Fundación
756 La Caixa (CX_E-2015-01).

757 We thank S. Bartlett (CNIC) for English editing and the members of the CNIC Transgenesis, Microscopy,
758 Genomics, Citometry, and Bioinformatic units. We also thank F. Alt (Boston Children's Hospital -
759 Harvard Medical School), T. Honjo (Kyoto University Institute for Advanced Studies), F. Radtke (Swiss
760 Institute for Experimental Cancer Research), R. H. Adams (Max Planck Institute for Molecular
761 Biomedicine), and R. De Pinho (MD Anderson Cancer Center) for sharing the *Myc* ^{floxed}, *Rbpj* ^{floxed},

762 *Notch1^{floxed}, Cdh5(PAC)-creER, and Foxos1/3/4^{floxed}* mice, respectively. We also thank Master's students
763 Joan Marc Arbonés and Alejandro Rivera Sánchez for their work on *iFlpMosaics*.

764

765 **Author contributions statement**

766 I.G-G. and R.B. designed most of the experiments, interpreted results, assembled figures, and wrote
767 the manuscript. R.B. designed all DNA vectors. I.G-G. did most of the DNA engineering (cloning),
768 CRISPR-Cas9 genome targeting, animal experiments, confocal microscopy, and FACS analysis. Mice
769 were generated by the CNIC Transgenesis Unit. S.G. developed new methods for *iFlpMosaics*
770 induction, tissue immunostaining, and multispectral microscopy imaging, performed animal
771 experiments and image analysis, and interpreted results. L.G-O, W.L., I.Z., and M.F-C. performed
772 animal experiments, FACS, histology, and confocal imaging. I.G-G and A.R analyzed scRNA-seq data.
773 A.R. cloned and validated the *iFlp/Dre^{Progenitor}* allele. S.F.R. performed image quantifications in Fiji and
774 graphpad, edited text and figures, and assembled figures. M.L, M.S.S-M, A.G.-C, F.L., and V.C-G gave
775 general technical assistance with experiments and genotyped the mouse colonies. All authors
776 approved the final version of the manuscript.

777

778 **Competing interests statement**

779 The authors declare no competing interests.

780

781 **Figure legends:**

782 **Figure 1: *iFlpMosaics* allow efficient and ratiometric labeling of mutant and wildtype cells. a,**
783 Schematic showing how a standard Cre-reporter can recombine and label cells without the deletion of
784 any floxed gene (G) (false positives) and how the floxed gene can be deleted in non-Cre-recombined
785 cells (false negatives). **b,** Different recombination efficiencies of Cre-reporters, despite all localizing to
786 the *Rosa26* locus and having a similar genetic distance between LoxP sites. **c,d,** Cre-reporters only
787 accurately report recombination of themselves, not that of other floxed alleles (reporters), particularly
788 at low tamoxifen doses. **e,** The novel R26-*iFlp$^{MTomato\text{-}Cre/MYFP}$* allele, in which Flpo/FlpOERT2-induced
789 recombination of the mutually exclusive FRTF3 and FT5T2 sites leads to one of two possible outcomes:
790 cells expressing MTomato and Cre (mutant) or cells expressing MYFP (wildtype) (see also Sup. Fig.
791 1). Induction leads to a ratiometric proportion of ~ 65%MTom+:35%MYFP+. **f**, Tg-*iFlp$^{MTomato\text{-}H2B\text{-}GFP\text{-}}$*
792 *$^{Cre/MYFP\text{-}H2B\text{-}Cherry\text{-}FlpO}$* allele and confocal micrographs showing the full spectral separation of the 4
793 fluorescent labels expressed in mutant and wildtype cells. **g,** In a wildtype background, the initial

794 ratiometric proportion of MTomato+ and MYFP+ cells is maintained throughout embryogenesis to
795 postnatal stages, indicating non-toxicity of Cre in MTomato+ cells. **h**, Comparison of MTomato
796 intensity and Cre expression in cells of R26-*iFlp*$^{MTomato\text{-}Cre/MYFP}$ and Tg(*iSure-Cre*) mice. **i,** Efficient
797 recombination of the Cre-reporter *Rosa26*$^{\text{-}LSL\text{-}YFP}$ in MTomato+ cells (white arrowheads) after induction
798 of the R26-*iFlp*$^{MTomato\text{-}Cre/MYFP}$ allele by *Apln-FlpO*. There are few false positives (red arrows). The charts
799 show representative FACS analysis of livers from the same animals and related numerical data from
800 livers and retinas. **j,** Combination of the *iFlp*$^{MTomato\text{-}Cre/MYFP}$ allele with other floxed genes leads to very
801 significant deletion of these in MTomato+ cells. **k,** Induction of *iFlp*$^{MTomato\text{-}Cre/MYFP}$ in mice carrying a
802 floxed allele for *Rbpj*, an essential gene for arterial development, results in only 3.5% Tomato-2A-Cre+
803 cells in arteries (A), versus 96% in veins (v) and capillaries. Data are presented as mean values +/- SD.
804 For statistics see Source Data File 1. Scale bars are 50µm.
805

806 **Figure2: Generation of ubiquitous and tissue-specific FlpoERT2 mouse lines. a,** Recombination of
807 the *iFlp*$^{MTomato\text{-}Cre/MYP}$ mosaic mouse lines induced by the published *R26*$^{CAG\text{-}FlpoERT2}$ allele leads to reduced
808 recombination efficiency at embryonic and postnatal stages and in adult organs. **b,** Schematic of novel
809 *Tg(Ins-CAG-FlpoERT2*) alleles containing DNA elements optimized to enhance FlpOERT2 expression.
810 **c,** Comparison of FlpO copy number by genomic DNA qRT-PCR. **d-g** Comparison by FACS and
811 histology of the recombination efficiency of the different FlpOERT2-expressing mouse lines/founders
812 at embryonic, postnatal, and adult stages. Fold change is indicated for the most significant changes. **h,**
813 Crispr/Cas9 targeting procedure for the generation of novel endothelial-specific *Cdh5-FlpoERT2-*
814 expressing mouse lines from the published *Cdh5-CreERT2* mouse line. **i,** Comparison of FlpO and Cre
815 copy number by genomic DNA qRT-PCR. **j,** Recombination efficiency of Founder #1 of the newly
816 generated *Tg(Cdh5-FlpoERT2)* mouse line in embryonic, postnatal, and adult tissues. Data are
817 presented as mean values +/- SD. For statistics see Source Data File 1. Scale bars, 100µm.
818
819

820 **Figure3: Ratiometric *iFlpMosaics* allow high-throughput assessment of a cell-autonomous gene**
821 **function. a,b,** *iFlp*$^{MTomato\text{-}Cre/MYP}$ mosaics were induced with *Apln-FlpO* (recombines endothelial and
822 derived hematopoietic cells at E9.5) on control (wildtype) and Myc floxed backgrounds, and tissues
823 were analyzed at P7. FACS data for CD31+ (ECs) and CD45+ (Blood) cells shows that *Myc* deletion
824 (in MTomato+ cells) leads to a competitive disadvantage, especially in blood cells. Absolute fold
825 change is indicated in red. **c,** When *iFlp*$^{MTomato\text{-}Cre/MYFP}$ mosaics are induced in most embryonic cells with
826 *ACTB:FlpE*, analysis of other organ cell types (CD31-CD45-) reveals that *Myc* is necessary for the
827 development of liver cells, but not lung or heart cells. **d,** *iFlp*$^{MTomato\text{-}Cre/MYP}$ mosaics were combined with
828 *Tg(Ins-CAG-FlpOERT2)* on control (wildtype) and *Foxo1/3/4* floxed backgrounds, and tamoxifen was
829 injected at P1 to induce recombination in all cell types. Liver, lung, and heart cells were analyzed at
830 P15 by FACS. *Foxo1/3/4* deletion (in MTomato+ cells) increases the proliferation of heart cells, but

not liver or lung cells. **e,** Representative confocal micrographs of control and *Foxo1/3/4* mosaic P6 and P15 retinas from animals induced at P1. The chart shows ratiometric analysis of retinal immunostainings for Tomato, YFP, and ERG (labels EC nuclei), showing that *Foxo1/3/4*^{KO} ECs have a competitive advantage. Data are presented as mean values +/- SD. For statistics see Source Data File 1. Scale bars are 100µm.

Figure 4: Combining *iFlpMosaic* with *iFlp*^{Chromatin} yields higher single-cell clonal resolution. a, Representative confocal micrograph of adult liver sections from mice carrying the *Tg(Ins-CAG-FlpoERT2), iFlp*$^{MTomato-Cre/MYFP}$, and *Rosa26-iChr2-Mosaic (iCre*$^{H2B-Cherry/GFP/Cerulean}$) alleles. Combination of these membrane and nuclear reporter alleles allows up to 3 mutant and 1 wildtype cell barcodes (labeling). Note that binucleated (2x2n) or polyploid (4n) hepatocytes can have more multispectral barcodes. **b,** Representative confocal micrograph of a P7 retina from an animal containing the *Tg(Ins-CAG-FlpOERT2)* allele and the new *iFlp*^{Chromatin} nuclear reporter allele (for explanations of similar DNA elements, see Sup. Fig.4c) induced at P1 with 4-OHT. The bar shows the ratiometric frequency of each nuclear/H2B+ fluorescent marker. **c,** Representative confocal micrograph of the indicated adult organ sections of animals carrying the *iFlp*^{Chromatin} and *Tg(Ins-CAG-FlpOERT2)* alleles. Mononucleated diploid cells (kidney and lung) express only 1 of 3 possible nuclear/chromatin markers, whereas multinucleated or polyploid cells (hepatocytes and cardiomyocytes) can express a combination of 2 or 3 possible markers (6 possible chromatin barcodes in total). **d,** Recombination and cell barcoding possibilities in animals carrying the indicated alleles. The representative confocal micrographs of a P7 retina show that wildtype and mutant cells can both be labeled in 4 different ways, significantly increasing single-cell clonal resolution. The panel to the right illustrates how a Fiji image analysis script automatically detects, segments, and pseudocolors the nuclei of dual-labeled cells (nuclei and membrane). **e,** Recombination and diploid cell barcoding possibilities in animals carrying the indicated alleles. The representative confocal micrographs of an adult liver (collected 2 weeks after tamoxifen induction) show that mutant hepatocytes can be labeled with up to 16 different fluorescent barcodes, depending on whether the cells are mononucleated (diploid) or multinucleated (polyploid). Wildtype hepatocytes can have up to 8 different fluorescent barcodes (only 6 shown). Scale bars, 100µm.

Figure 5: High-resolution *iFlpMosaics* reveal the impact of genetic mutations on single-cell clonal dynamics. a, Quantification of Ki67+ cells (in cycle) and EdU+ cells (S-phase) in P1, P7, and P20 livers. **b,** *Left* Schematic of the indicated alleles combined in a single animal and how they can be used to fluorescently barcode and track the clonal expansion of single mutant and wildtype cells from P1 to P20. *Right* Representative confocal micrographs of P20 livers (from animals induced with 4-OHT at P1) with different recombination frequencies (see also Sup. Fig. 5). **c,** Clone size distributions at both low and high recombination rates. Recombination frequency and fluorescent barcoding density

867 do not affect clonal resolution and quantification. **d,** Liver weight at P1 and P20. **e,** Quantification of
868 MYFP+ (*Myc*^{WT}) and MTomato+ (*Myc*^{KO}) clone size frequency, showing that *Myc*^{KO} hepatocytes
869 divide less. **f,** Chart depicting the normalized expansion of *Myc*^{WT} and *Myc*^{KO} hepatocytes over the
870 same 20-day period. **g,** Representative confocal micrographs of P20 pancreas from control and *Myc*-
871 floxed mice carrying the indicated *iFlpMosaic* alleles. Right panels are inverted LUT images
872 depicting the clone mapping (Fiji image analysis scripts) according to their dual color code. **h,**
873 Quantification of MYFP+ (*Myc*^{WT}) and MTomato+ (*Myc*^{KO}) clone size frequency, showing that *Myc*^{KO}
874 pancreatic cells divide less. **i,** Chart depicting the normalized expansion of *Myc*^{WT} and *Myc*^{KO}
875 pancreatic cells over the same 20-day period. **j,** Log2 ratio of Tom+ cells to YFP+ cells in control and
876 *Myc*-floxed pancreas, showing a 3.7 fold loss of MTomato+ (*Myc*^{KO}) cells over 20 days. **k,**
877 Representative confocal micrographs of adult livers from control and *Myc*-floxed mice in which the
878 indicated *iFlpMosaic* and *iCre*$^{Mb2\text{-}Mosaic}$ alleles were induced 14 days before tissue collection. Right
879 panels show automatic mapping of clones (Fiji image analysis scripts) according to their fluorescent
880 barcode. Note the loss of MTomato+ cells in the *Myc*-floxed background. **l,** Clone size, showing that
881 wildtype hepatocytes rarely divide or expand over a 2-week period. **m,** Clone frequency of wildtype
882 MYFP+ and MTomato+ hepatocyte clones, showing the lack of impact of Cre expression in
883 MTomato+ cells. Note the difference between diploid, mononucleated, polynucleated, and polyploid
884 cells. **n,** Percentages of proliferative (composed of more than 1 cell) and non-proliferative YFP+ and
885 Tomato+ clones, showing no major difference between the two wildtype populations. **o,** Log2 ratio of
886 the Tom+ and YFP+ cell frequency in control and adult *Myc*-floxed livers, showing loss of a large
887 fraction of *Myc*^{KO} cells over 2 weeks. **p,** Clone frequency of YFP+ (*Myc*^{WT}) and Tomato+ (*Myc*^{KO})
888 hepatocytes, showing that the surviving *Myc*^{KO} population contains an increased frequency of non-
889 proliferating binucleated cells and a decrease frequency of proliferating mononucleated cells. **q,**
890 Percentages of proliferative and non-proliferative YFP+ (*Myc*^{WT}) and Tomato+ (*Myc*^{KO}) clones,
891 showing that loss of *Myc* reduces proliferative-clone frequency.

892 **Figure 6: *iFlp/Dre*^{Progenitor} enables the induction of genetic mosaics in the progeny of single cells.**
893 **a,** Schematic of the *iFlp/Dre*^{Progenitor} DNA construct used to generate transgenic mice. **b,** Generation of
894 *Tg(Ins-CAG-DreERT2)* by CRISPR-Cas9 mediated replacement of FlpO by Dre in the existing
895 *Tg(Ins-CAG-FlpOERT2)*^{F4} allele. **c**, Schematic of the genetic cascade induced in animals containing
896 the indicated alleles. After tamoxifen induction of FlpOERT2 or DreERT2, the *iFlp/Dre*^{Progenitor} allele
897 is recombined, driving expression of the nuclear marker H2B-V5, the surface marker truncated human
898 CD2 (hCD2), and FlpO. FlpO is a relatively weak recombinase that needs to be expressed and
899 accumulate in the cell before it recombines the *iFlp*$^{MTomato\text{-}Cre/MYFP}$ allele. This delay results in
900 recombination in the progeny of a single progenitor cell. **d**,**e**, In animals lacking the *iFlp/Dre*^{Progenitor}
901 allele, most single-cell derived clones are formed by just one type of cell (MTomato+ or MYFP+).
902 With the *iFlp/Dre*^{Progenitor} allele, it is possible to induce clones formed by mutant (MTomato+) and

903 wildtype (MYFP+) cells derived from single progenitor cells (see also Sup. Fig. 6). **f**, Retinal confocal
904 micrographs showing that the *iFlp/Dre*^{Progenitor} allele significantly increases the recombination
905 frequency of *iFlp*$^{MTomato\text{-}Cre/MYFP}$ (induced at P3 and collected at P7), enabling high frequency genetic
906 mosaics with the weaker *Cdh5-FlpOERT2* line (expressed only in Cdh5+ ECs). H2B-V5 labels the
907 nuclei of cells recombining and expressing the *iFlp/Dre*^{Progenitor} allele. **g**, FACS plots showing that the
908 *iFlp/Dre*^{Progenitor} allele significantly increases the recombination frequency of the *iFlp*$^{MTomato\text{-}Cre/MYFP}$
909 allele when combined with the *Tg(Ins-CAG-FlpOERT2)* allele. **h**, Retinal confocal micrographs
910 showing that combination of the new *Tg(Ins-CAG-DreERT2)* line with the *iFlp/Dre*^{Progenitor} allele
911 increases the recombination fequency of the *iFlp*$^{MTomato\text{-}Cre/MYFP}$ allele. H2B-V5 labels the nuclei of
912 cells recombining and expressing the *iFlp/Dre*^{Progenitor} allele.
913
914 **Figure 7: Combining single-cell RNA-seq with ratiometric *iFlpMosaics* to reveal cell-autonomous**
915 **gene function. a,** Schematic of the induction of the indicated alleles at E9.5 and collection of cells at
916 E13.5 by FACS for scRNA-seq. **b**, Umaps showing the spatial distribution of the *Rbpj*^{KO} (MTomato+)
917 and *Rbpj*^{Wt} (MYFP+) cells and the different clusters they form. The dot plot on the right shows the top
918 markers used to identify the major cell types. **c**, Dot plot showing the frequency and amplitude of
919 expression for *Rbpj,* the canonical Notch target *Hes1*, and the G2/M phase (proliferation) marker *MKi67*
920 in wildtype cells (MYFP+) and mutant cells (MTomato-2A-Cre+). Note that *Rbpj* deletion only
921 removes exons 6 and 7, leaving the 3´mRNA intact. However, this truncated mRNA is less stable and
922 less detectable after deletion. **d**,**e**, Histobars and Umap showing that mosaic deletion of *Rbpj*
923 (MTomato+ cells) changes the relative proportion of different cell types. **f-r**, Umaps showing the cell-
924 type specific subclusters, together with top dysregulated marker genes and gene-set-enrichment analysis
925 charts, showing how *Rbpj* deletion changes the frequency, differentiation, and biology of the indicated
926 cell types.

927 **Supplementary Figure 1: *iFlpMosaics* are neither toxic nor leaky**

928 **a, b,** Schematic diagrams of the novel Rosa26-*iFlp*$^{MTomato\text{-}Cre/MYFP}$ and Tg-*iFlp*$^{MTomato\text{-}H2B\text{-}GFP\text{-}Cre/MYFP\text{-}H2B\text{-}}$
929 $^{Cherry\text{-}FlpO}$ alleles, showing the genetic distances between the mutually exclusive FRT site pairs and the
930 expected outcomes after FlpO/FlpOERT2 recombination. **c, d** Confocal microscopy and FACS
931 analysis of mouse ES cells used to generate Rosa26-*iFlp*$^{MTomato\text{-}Cre/MYFP}$ mice 3 days after transfection
932 with FlpO-expressing plasmids. **e-g**, Frequency of recombination and expression detected by
933 microscopy in ES cells and ECs derived from embryoid bodies (EBs). **h**, Relative frequency of
934 MTomato-2A-Cre+ and MYFP+ cells in ES cells (in vitro) and in blood (in vivo); the absence of
935 change over time shows that permanent expression of Cre is non-toxic to cells. **i**, FACS analysis of
936 FlpO versus Cre-dependent leakiness in adult organs of mice carrying the standard *Rosa26-LSL-YFP*
937 allele in combination with *iFlpMosaics* alleles. FlpO leakiness was not detected (0% Tomato+ cells),
938 and Cre-non-self-leakiness (only detectable with the additional *Rosa26-LSL-YFP* allele) was observed

939 only in a very small fraction of cells from animals carrying the Tg-*iFlp*$^{MTomato\text{-}H2B\text{-}GFP\text{-}Cre/MYFP\text{-}H2B\text{-}Cherry\text{-}FlpO}$
940 allele and not at all in animals carrying the Rosa26-*iFlp*$^{MTomato\text{-}Cre/MYFP}$ allele.

941 **Supplementary Figure 2: Validation of *iFlpMosaics* for ratiometric quantitative gene function**
942 **analysis. a,** Representative confocal micrographs of a P6 retina from a *Rbpj*-floxed mouse carrying the
943 *iFlp*$^{MTomato\text{-}Cre/MYFP}$ and *Apln-FlpO* alleles. *Apln* is an X-chromosomal gene (mosaicly expressed in
944 females) expressed at the angiogenic front of growing vessels, recombining in angiogenic front ECs
945 that later form the entire vasculature. *Apln* also recombines in non-endothelial (ERG-negative) cells in
946 the retina. The right micrograph shows ERG-signal segmentation (EC nuclei), with nuclei of Tomato+
947 (*Rbpj*^{KO}) cells in red and nuclei of YFP+ (*Rbpj*^{WT}) cells in green. Grey nuclei are in non-recombined
948 ERG+ cells. Dashed white lines demark the leading edge (LE), angiogenic front (AF), and mature area
949 (MA). A, arteries; V, veins. The chart shows the log2 ratios of Tomato+ to YFP+ ECs in each retinal
950 region, showing the enrichment of *Rbpj*^{KO} cells in the LE and AF, which suggests a role for this gene
951 in cell migration to the front of the plexus. **b, c** Representative confocal micrographs of a P6 retina from
952 *Rbpj*-floxed mouse carrying the *iFlp*$^{MTomato\text{-}H2BGFP\text{-}Cre/MYFP\text{-}H2BCherry}$ and *Apln-FlpO* alleles. This allows
953 the nuclear labeling of *Rbpj*^{KO} (H2B-GFP+) and *Rbpj*^{Wt} (H2B-Cherry+) ECs and blood cells, which is
954 more convenient for cell object segmentation and quantification of nuclear-specific proteins, such as
955 the proliferation and cell-cycle arrest markers Ki67 and p21. Nuclear segmentation outlines: red,
956 Cherry+/Ki67- or p21-; pink, Cherry+/Ki67+ or p21+; green, GFP+/Ki67- or p21-; cyan, GFP+/Ki67+
957 or p21+. Scale bars, 150μm.

958 **Supplementary Figure 3: Comparative analysis of recombination efficiency in FlpOERT2 mouse**
959 **lines. a-c,** Representative FACs plots of different adult organs, showing YFP+ and Tomato+ cell
960 frequencies in from mice carrying the *iFlp*$^{MTomato\text{-}Cre/MYFP}$ allele in combination with the published
961 *R26*$^{CAG\text{-}FlpoERT2}$ or the newly generated *Tg(Ins-CAG-FlpoERT2)*^{F2} allele. **d,** Confocal micrograph of a
962 flat-mounted adult mouse aorta 2 weeks after induction. **e,** FACS analysis showing the lack of leakiness
963 of the *Tg(Ins-CAG-FlpoERT2)*^{F2} allele. In the absence of tamoxifen, the *iFlp*$^{MTomato\text{-}Cre/MYFP}$ allele is not
964 recombined.
965

966 **Supplementary Figure 4: Ratiometric iFlpMosaics reveal that the competitive disadvantage of**
967 ***Myc*^{KO} cells is stronger in blood cells than in ECs. a,b,** Representative FACS plots showing that in
968 both the heart and the lung CD45+ blood cells are much more affected by *Myc* deletion than CD31+
969 ECs. **c**, Schematic diagram of the *iChr2-Mosaic* construct (also called *iCre*$^{H2B\text{-}Cherry/GFP/Cerulean}$) targeted
970 to the Rosa26 locus and having 4 insulator (INS) sequences and the strong and ubiquituous CAG
971 enhancer/promoter. N-PhiMut encodes a non-fluorescent nuclear marker protein detectable with an
972 antibody. It is expressed before Cre recombination. After Cre-mediated recombination between
973 compatible pairs of LoxP sites, only one of the 3 possible fluorescent proteins will be expressed. WPRE,

974 woodchuck hepatitis virus post-transcriptional regulatory element, used to enhance transgene
975 expression. pA, Sv40 polyA, used to terminate transcription.

976 **Supplementary Figure 5: Mapping the clonal expansion of single mutant and wildtype cells with**
977 ***iFlpMosaics*. a,b,** Representative confocal images (low magnification large tile scans) of entire P20
978 liver sections from mice carrying the indicated alleles. Recombination of the reporter alleles was
979 induced at P1 and resulted in different recombination frequencies. Right panels show the results of
980 automatic image processing with Fiji scripts, which generate spatial maps of dual-labeled clones of cells
981 (with membrane and nuclear labeling). The bigger the circle, the bigger the clone. **c,** Quantification and
982 representative confocal micrographs of proliferative pancreatic cells (Ki67+ in cycle or EdU+ in s-
983 phase) at different postnatal stages. **d,** Quantification and representative confocal micrograph of
984 Ki67+/DAPI+ cells in the adult liver. **e,** Representative confocal micrographs of adult liver sections
985 from control and *Myc*-floxed mice carrying the indicated alleles. Left panels show endogenous
986 fluorescent signals from the reporter alleles. Center panels show sections from the same mice
987 immunostained with antibodies to DsRed (detects MTomato and H2B-Cherry), GFP (detects MYFP
988 and H2B-GFP), or the HA epitope (detects MTFP1 and H2B-Cerulean) together with Fiji-script-
989 generated spatial maps of dual-labeled clones (with membrane and nuclear labeling) reveal hepatocyte
990 ploidy and clone size. Graphs show the percentages of mononucleated cells, binucleated cells, and 2-
991 cell mononuclear clones. In control mice, MYFP+ (WT) and MTomato+ (WT) diploid cells occur in
992 similar proportions, whereas in *Myc*-floxed mutants MTomato+ (Myc^{KO}) diploid cells are more
993 frequently binucleated and give rise to fewer 2-cell mononucleated clones than MYFP+ (Myc^{WT}) cells.

994 **Supplementary Figure 6: *iFlp/Dre*^{Progenitor} enables the induction of genetic mosaics from a single**
995 **progenitor cell. a,** Representative confocal micrograph of a P7 retina from an animal carrying the
996 indicated alleles and induced with 4-OHT at P3. After induction of the ***iFlp/Dre***^{Progenitor} allele, cells
997 express the nuclear marker H2B-V5 and FlpO. After some rounds of cell division, FlpO will recombine
998 the $iFlp^{MTomato\text{-}Cre/MYFP}$ allele, generating MYFP+ and MTomato+ progeny cells derived from a single
999 initial recombination event.

1000 **Supplementary Figure 7: Single cell RNA-seq analysis combined with ratiometric iFlpMosaics**
1001 **uncovers cell-autonomous gene function in diverse cell types.**

1002 **a,** Umaps and barplots showing the identified clusters and their frequencies among YFP+ ($Rbpj^{WT}$) and
1003 Tomato+ ($Rbpj^{KO}$) cells. **b,** Dot plots showing the frequency (size) and expression level (color intensity)
1004 for the top cluster marker genes. **c,** Top differentially expressed genes per cluster between YFP+
1005 ($Rbpj^{WT}$) and Tomato+ ($Rbpj^{KO}$) cells. Most of the charts also show the expression of *Rbpj*, its canonical
1006 target *Hes1*, and the proliferation markers *Ki67* (G2/M cells) and *Cdkn1a* (arrested cells). **d,** Gene set
1007 enrichment analysis (GSEA) pathways with their normalized enrichment score. For some cell types
1008 there are no differentially expressed genes or pathways.

1009 **References**

1010

1011 Aran, D., Looney, A.P., Liu, L., Wu, E., Fong, V., Hsu, A., Chak, S., Naikawadi, R.P., Wolters, P.J., Abate,
1012 A.R., et al. (2019). Reference-based analysis of lung single-cell sequencing reveals a
1013 transitional profibrotic macrophage. Nat Immunol *20*, 163-172. 10.1038/s41590-018-0276-y.
1014 Cai, D., Cohen, K.B., Luo, T., Lichtman, J.W., and Sanes, J.R. (2013). Improved tools for the Brainbow
1015 toolbox. Nature methods *10*, 540-547.
1016 Claveria, C., Giovinazzo, G., Sierra, R., and Torres, M. (2013). Myc-driven endogenous cell
1017 competition in the early mammalian embryo. Nature *500*, 39-44. 10.1038/nature12389.
1018 Contreras, X., Amberg, N., Davaatseren, A., Hansen, A.H., Sonntag, J., Andersen, L., Bernthaler, T.,
1019 Streicher, C., Heger, A., Johnson, R.L., et al. (2021). A genome-wide library of MADM mice for
1020 single-cell genetic mosaic analysis. Cell reports *35*, 109274. 10.1016/j.celrep.2021.109274.
1021 de Alboran, I.M., O'Hagan, R.C., Gartner, F., Malynn, B., Davidson, L., Rickert, R., Rajewsky, K.,
1022 DePinho, R.A., and Alt, F.W. (2001). Analysis of C-MYC function in normal cells via
1023 conditional gene-targeted mutation. Immunity *14*, 45-55.
1024 Dharaneeswaran, H., Abid, M.R., Yuan, L., Dupuis, D., Beeler, D., Spokes, K.C., Janes, L., Sciuto, T.,
1025 Kang, P.M., Jaminet, S.S., et al. (2014). FOXO1-mediated activation of Akt plays a critical role
1026 in vascular homeostasis. Circ Res *115*, 238-251. 10.1161/CIRCRESAHA.115.303227.
1027 Eijkelenboom, A., and Burgering, B.M. (2013). FOXOs: signalling integrators for homeostasis
1028 maintenance. Nat Rev Mol Cell Biol *14*, 83-97. 10.1038/nrm3507.
1029 Ema, M., Takahashi, S., and Rossant, J. (2006). Deletion of the selection cassette, but not cis-acting
1030 elements, in targeted Flk1-lacZ allele reveals Flk1 expression in multipotent mesodermal
1031 progenitors. Blood *107*, 111-117. 10.1182/blood-2005-05-1970.
1032 Fernandez-Chacon, M., Casquero-Garcia, V., Luo, W., Francesca Lunella, F., Ferreira Rocha, S., Del
1033 Olmo-Cabrera, S., and Benedito, R. (2019). iSuRe-Cre is a genetic tool to reliably induce and
1034 report Cre-dependent genetic modifications. Nature communications *10*, 2262.
1035 10.1038/s41467-019-10239-4.
1036 Han, H., Tanigaki, K., Yamamoto, N., Kuroda, K., Yoshimoto, M., Nakahata, T., Ikuta, K., and Honjo, T.
1037 (2002). Inducible gene knockout of transcription factor recombination signal binding protein-
1038 J reveals its essential role in T versus B lineage decision. Int Immunol *14*, 637-645.
1039 Hansen, A.H., and Hippenmeyer, S. (2020). Non-Cell-Autonomous Mechanisms in Radial Projection
1040 Neuron Migration in the Developing Cerebral Cortex. Front Cell Dev Biol *8*, 574382.
1041 10.3389/fcell.2020.574382.
1042 Hansen, A.H., Pauler, F.M., Riedl, M., Streicher, C., Heger, A., Laukoter, S., Sommer, C., Nicolas, A.,
1043 Hof, B., Tsai, L.H., et al. (2022). Tissue-Wide Effects Override Cell-Intrinsic Gene Function in
1044 Radial Neuron Migration. Oxford Open Neuroscience *1*. 10.1093/oons/kvac009.
1045 Hao, Y., Hao, S., Andersen-Nissen, E., Mauck, W.M., 3rd, Zheng, S., Butler, A., Lee, M.J., Wilk, A.J.,
1046 Darby, C., Zager, M., et al. (2021). Integrated analysis of multimodal single-cell data. Cell *184*,
1047 3573-3587 e3529. 10.1016/j.cell.2021.04.048.
1048 He, C., Hu, H., Braren, R., Fong, S.-Y., Trumpp, A., Carlson, T.R., and Wang, R.A. (2008). c-myc in the
1049 hematopoietic lineage is crucial for its angiogenic function in the mouse embryo.
1050 Development *135*, 2467-2477. 10.1242/dev.020131.
1051 He, L., Pu, W., Liu, X., Zhang, Z., Han, M., Li, Y., Huang, X., Han, X., Li, Y., Liu, K., et al. (2021).
1052 Proliferation tracing reveals regional hepatocyte generation in liver homeostasis and repair.
1053 Science *371*, eabc4346. doi:10.1126/science.abc4346.
1054 Hunter, N.L., Awatramani, R.B., Farley, F.W., and Dymecki, S.M. (2005). Ligand-activated Flpe for
1055 temporally regulated gene modifications. Genesis *41*, 99-109. 10.1002/gene.20101.
1056 Knoepfler, P.S., Cheng, P.F., and Eisenman, R.N. (2002). N-myc is essential during neurogenesis for
1057 the rapid expansion of progenitor cell populations and the inhibition of neuronal
1058 differentiation. Genes Dev *16*, 2699-2712. 10.1101/gad.1021202.

1059 Kranz, A., Fu, J., Duerschke, K., Weidlich, S., Naumann, R., Stewart, A.F., and Anastassiadis, K. (2010).
1060 An improved Flp deleter mouse in C57Bl/6 based on Flpo recombinase. Genesis *48*, 512-520.
1061 10.1002/dvg.20641.
1062 Lao, Z., Raju, G.P., Bai, C.B., and Joyner, A.L. (2012). MASTR: a technique for mosaic mutant analysis
1063 with spatial and temporal control of recombination using conditional floxed alleles in mice.
1064 Cell reports *2*, 386-396. 10.1016/j.celrep.2012.07.004.
1065 Liu, J., Willet, S.G., Bankaitis, E.D., Xu, Y., Wright, C.V., and Gu, G. (2013). Non-parallel recombination
1066 limits cre-loxP-based reporters as precise indicators of conditional genetic manipulation.
1067 Genesis *51*, 436-442. 10.1002/dvg.22384.
1068 Livet, J., Weissman, T.A., Kang, H., Draft, R.W., Lu, J., Bennis, R.A., Sanes, J.R., and Lichtman, J.W.
1069 (2007). Transgenic strategies for combinatorial expression of fluorescent proteins in the
1070 nervous system. Nature *450*, 56-62. nature06293 [pii]

1071 10.1038/nature06293.
1072 Loonstra, A., Vooijs, M., Beverloo, H.B., Allak, B.A., van Drunen, E., Kanaar, R., Berns, A., and Jonkers,
1073 J. (2001). Growth inhibition and DNA damage induced by Cre recombinase in mammalian
1074 cells. Proc Natl Acad Sci U S A *98*, 9209-9214. 10.1073/pnas.161269798.
1075 Luo, W., Garcia-Gonzalez, I., Fernández-Chacón, M., Casquero-Garcia, V., Sanchez-Muñoz, M.S.,
1076 Mühleder, S., Garcia-Ortega, L., Andrade, J., Potente, M., and Benedito, R. (2021).
1077 Arterialization requires the timely suppression of cell growth. Nature *589*, 437-441.
1078 10.1038/s41586-020-3018-x.
1079 Madisen, L., Zwingman, T.A., Sunkin, S.M., Oh, S.W., Zariwala, H.A., Gu, H., Ng, L.L., Palmiter, R.D.,
1080 Hawrylycz, M.J., Jones, A.R., et al. (2010). A robust and high-throughput Cre reporting and
1081 characterization system for the whole mouse brain. Nat Neurosci *13*, 133-140.
1082 10.1038/nn.2467.
1083 Munoz-Martin, N., Sierra, R., Schimmang, T., Villa Del Campo, C., and Torres, M. (2019). Myc is
1084 dispensable for cardiomyocyte development but rescues Mycn-deficient hearts through
1085 functional replacement and cell competition. Development *146*. 10.1242/dev.170753.
1086 Naiche, L.A., and Papaioannou, V.E. (2007). Cre activity causes widespread apoptosis and lethal
1087 anemia during embryonic development. Genesis *45*, 768-775. 10.1002/dvg.20353.
1088 Paik, J.H., Kollipara, R., Chu, G., Ji, H., Xiao, Y., Ding, Z., Miao, L., Tothova, Z., Horner, J.W., Carrasco,
1089 D.R., et al. (2007). FoxOs are lineage-restricted redundant tumor suppressors and regulate
1090 endothelial cell homeostasis. Cell *128*, 309-323. 10.1016/j.cell.2006.12.029.
1091 Pontes-Quero, S., Fernández-Chacón, M., Luo, W., Lunella, F.F., Casquero-Garcia, V., Garcia-
1092 Gonzalez, I., Hermoso, A., Rocha, S.F., Bansal, M., and Benedito, R. (2019). High mitogenic
1093 stimulation arrests angiogenesis. Nature communications *10*, 2016. 10.1038/s41467-019-
1094 09875-7.
1095 Pontes-Quero, S., Heredia, L., Casquero-Garcia, V., Fernandez-Chacon, M., Luo, W., Hermoso, A.,
1096 Bansal, M., Garcia-Gonzalez, I., Sanchez-Munoz, M.S., Perea, J.R., et al. (2017). Dual
1097 ifgMosaic: A Versatile Method for Multispectral and Combinatorial Mosaic Gene-Function
1098 Analysis. Cell *170*, 800-814 e818. 10.1016/j.cell.2017.07.031.
1099 Radtke, F., Wilson, A., Stark, G., Bauer, M., van Meerwijk, J., MacDonald, H.R., and Aguet, M. (1999).
1100 Deficient T Cell Fate Specification in Mice with an Induced Inactivation of Notch1. Immunity
1101 *10*, 547-558. 10.1016/s1074-7613(00)80054-0.
1102 Rashbrook, V.S., Brash, J.T., and Ruhrberg, C. (2022). Cre toxicity in mouse models of cardiovascular
1103 physiology and disease. Nature Cardiovascular Research *1*, 806-816. 10.1038/s44161-022-
1104 00125-6.
1105 Rodriguez, C.I., Buchholz, F., Galloway, J., Sequerra, R., Kasper, J., Ayala, R., Stewart, A.F., and
1106 Dymecki, S.M. (2000). High-efficiency deleter mice show that FLPe is an alternative to Cre-
1107 loxP. Nat Genet *25*, 139-140.
1108 Schmidt-Supprian, M., and Rajewsky, K. (2007). Vagaries of conditional gene targeting. Nat Immunol
1109 *8*, 665-668. 10.1038/ni0707-665.

1110 Sharma, P., Yan, F., Doronina, V.A., Escuin-Ordinas, H., Ryan, M.D., and Brown, J.D. (2012). 2A
1111 peptides provide distinct solutions to driving stop-carry on translational recoding. Nucleic
1112 Acids Res *40*, 3143-3151. 10.1093/nar/gkr1176.
1113 Siebel, C., and Lendahl, U. (2017). Notch Signaling in Development, Tissue Homeostasis, and Disease.
1114 Physiol Rev *97*, 1235-1294. 10.1152/physrev.00005.2017.
1115 Snippert, H.J., van der Flier, L.G., Sato, T., van Es, J.H., van den Born, M., Kroon-Veenboer, C., Barker,
1116 N., Klein, A.M., van Rheenen, J., Simons, B.D., and Clevers, H. (2010). Intestinal crypt
1117 homeostasis results from neutral competition between symmetrically dividing Lgr5 stem
1118 cells. Cell *143*, 134-144. 10.1016/j.cell.2010.09.016.
1119 Srinivas, S., Watanabe, T., Lin, C.S., William, C.M., Tanabe, Y., Jessell, T.M., and Costantini, F. (2001).
1120 Cre reporter strains produced by targeted insertion of EYFP and ECFP into the ROSA26 locus.
1121 BMC Dev Biol *1*, 4.
1122 Wang, Y., Nakayama, M., Pitulescu, M.E., Schmidt, T.S., Bochenek, M.L., Sakakibara, A., Adams, S.,
1123 Davy, A., Deutsch, U., Luthi, U., et al. (2010). Ephrin-B2 controls VEGF-induced angiogenesis
1124 and lymphangiogenesis. Nature *465*, 483-486. nature09002 [pii]

1125 10.1038/nature09002.
1126 Wei, Y., Wang, Y.G., Jia, Y., Li, L., Yoon, J., Zhang, S., Wang, Z., Zhang, Y., Zhu, M., Sharma, T., et al.
1127 (2021). Liver homeostasis is maintained by midlobular zone 2 hepatocytes. Science *371*.
1128 10.1126/science.abb1625.
1129 Wilhelm, K., Happel, K., Eelen, G., Schoors, S., Oellerich, M.F., Lim, R., Zimmermann, B., Aspalter,
1130 I.M., Franco, C.A., Boettger, T., et al. (2016). FOXO1 couples metabolic activity and growth
1131 state in the vascular endothelium. Nature *529*, 216-220. 10.1038/nature16498.
1132 Zong, H. (2014). Generation and applications of MADM-based mouse genetic mosaic system.
1133 Methods Mol Biol *1194*, 187-201. 10.1007/978-1-4939-1215-5_10.
1134 Zong, H., Espinosa, J.S., Su, H.H., Muzumdar, M.D., and Luo, L. (2005). Mosaic analysis with double
1135 markers in mice. Cell *121*, 479-492. 10.1016/j.cell.2005.02.012.

1136

1137

1138

1139

Figure 1

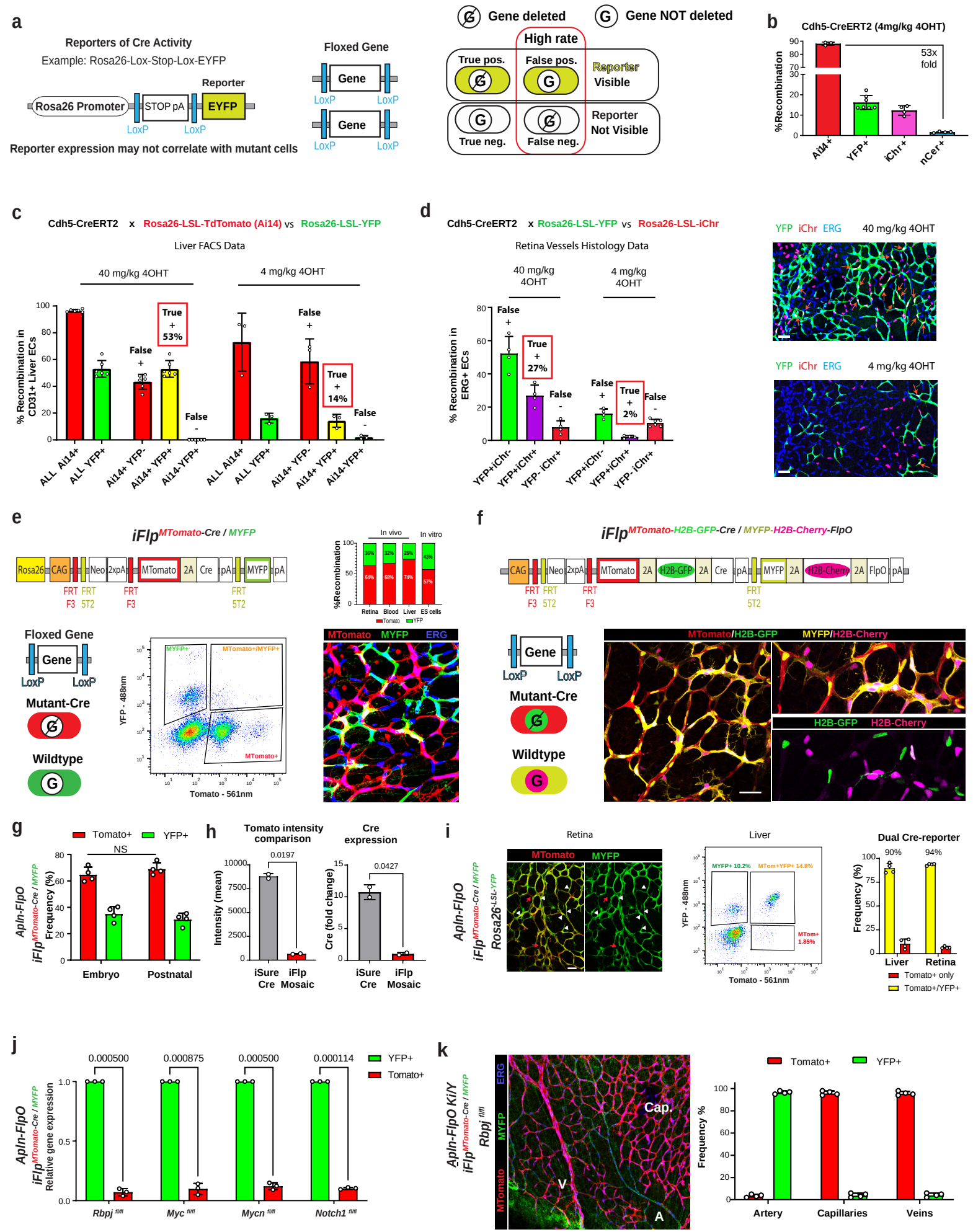
a
Reporters of Cre Activity
Example: Rosa26-Lox-Stop-Lox-EYFP
Rosa26 Promoter
STOP pA
EYFP
Reporter
LoxP
Floxed Gene
Gene
Reporter expression may not correlate with mutant cells
Gene deleted
Gene NOT deleted
High rate
True pos.
False pos.
Reporter Visible
True neg.
False neg.
Reporter Not Visible
b
Cdh5-CreERT2 (4mg/kg 4OHT)
%Recombination
53x fold
Ai14+
YFP+
iChr+
nCer+
c
Cdh5-CreERT2 x Rosa26-LSL-TdTomato (Ai14) vs Rosa26-LSL-YFP
Liver FACS Data
40 mg/kg 4OHT
4 mg/kg 4OHT
% Recombination in CD31+ Liver ECs
True + 53%
False +
False -
True + 14%
ALL Ai14+
ALL YFP+
Ai14+ YFP-
Ai14+ YFP+
Ai14-YFP+
d
Cdh5-CreERT2 x Rosa26-LSL-YFP vs Rosa26-LSL-iChr
Retina Vessels Histology Data
% Recombination in ERG+ ECs
True + 27%
True + 2%
YFP+iChr-
YFP+iChr+
YFP- iChr+
YFP iChr ERG
40 mg/kg 4OHT
4 mg/kg 4OHT
e
iFlpMTomato-Cre / MYFP
Rosa26
CAG
Neo
2xpA
MTomato
2A
Cre
pA
MYFP
FRT
F3
5T2
In vivo
In vitro
%Recombination
Retina
Blood
Liver
ES cells
Tomato
YFP
Floxed Gene
Gene
LoxP
Mutant-Cre
Wildtype
MYFP+
MTomato+/MYFP+
MTomato+
YFP - 488nm
Tomato - 561nm
MTomato MYFP ERG
f
iFlpMTomato-H2B-GFP-Cre / MYFP-H2B-Cherry-FlpO
H2B-GFP
H2B-Cherry
FlpO
MTomato/H2B-GFP
MYFP/H2B-Cherry
g
Tomato+
YFP+
NS
Apln-FlpO
iFlpMTomato-Cre / MYFP
Frequency (%)
Embryo
Postnatal
h
Tomato intensity comparison
Cre expression
0.0197
0.0427
Intensity (mean)
Cre (fold change)
iSure Cre
iFlp Mosaic
i
Retina
Liver
Dual Cre-reporter
Rosa26LSL-YFP
MTomato
MYFP
MYFP+ 10.2%
MTom+YFP+ 14.8%
MTom+ 1.85%
90%
94%
Tomato+ only
Tomato+/YFP+
j
0.000500
0.000875
0.000500
0.000114
Relative gene expression
Rbpj fl/fl
Myc fl/fl
Mycn fl/fl
Notch1 fl/fl
k
Apln-FlpO Ki/Y
iFlpMTomato-Cre / MYFP
Rbpj fl/fl
ERG
MYFP
MTomato
Cap.
V
A
Frequency %
Artery
Capillaries
Veins

Figure 2

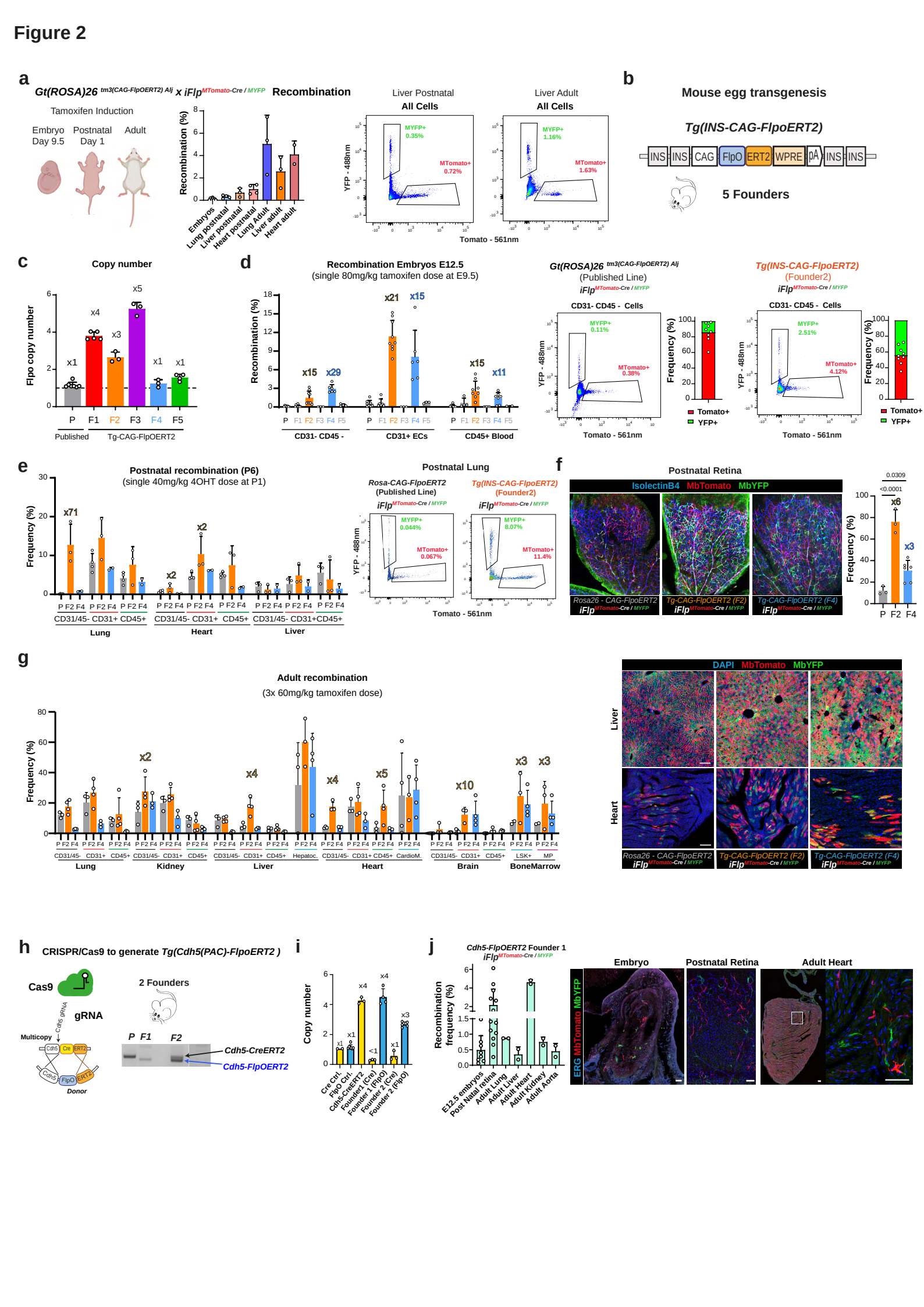
a
Gt(ROSA)26 tm3(CAG-FlpOERT2) Alj x iFlpMTomato-Cre / MYFP
Recombination
Tamoxifen Induction
Embryo Day 9.5
Postnatal Day 1
Adult
Recombination (%)
Embryos
Lung postnatal
Liver postnatal
Heart postnatal
Lung Adult
Liver adult
Heart adult
Liver Postnatal
All Cells
Liver Adult
All Cells
MYFP+ 0.35%
MTomato+ 0.72%
MYFP+ 1.16%
MTomato+ 1.63%
YFP - 488nm
Tomato - 561nm
b
Mouse egg transgenesis
Tg(INS-CAG-FlpoERT2)
INS INS CAG FlpO ERT2 WPRE bA INS INS
5 Founders
c
Copy number
Flpo copy number
x1 x4 x3 x5 x1 x1
P F1 F2 F3 F4 F5
Published
Tg-CAG-FlpOERT2
d
Recombination Embryos E12.5
(single 80mg/kg tamoxifen dose at E9.5)
Recombination (%)
x15 x29 x21 x15 x15 x11
CD31- CD45 -
CD31+ ECs
CD45+ Blood
Gt(ROSA)26 tm3(CAG-FlpOERT2) Alj
(Published Line)
iFlpMTomato-Cre / MYFP
Tg(INS-CAG-FlpoERT2)
(Founder2)
iFlpMTomato-Cre / MYFP
CD31- CD45 - Cells
MYFP+ 0.11%
MTomato+ 0.38%
MYFP+ 2.51%
MTomato+ 4.12%
Frequency (%)
Tomato+
YFP+
e
Postnatal recombination (P6)
(single 40mg/kg 4OHT dose at P1)
Frequency (%)
x71 x2 x2
CD31/45- CD31+ CD45+
Lung
Heart
Liver
Postnatal Lung
Rosa-CAG-FlpoERT2
(Published Line)
Tg(INS-CAG-FlpoERT2)
(Founder2)
iFlpMTomato-Cre / MYFP
MYFP+ 0.044%
MTomato+ 0.067%
MYFP+ 8.07%
MTomato+ 11.4%
f
Postnatal Retina
IsolectinB4 MbTomato MbYFP
Rosa26 - CAG-FlpoERT2
Tg-CAG-FlpOERT2 (F2)
Tg-CAG-FlpOERT2 (F4)
iFlpMTomato-Cre / MYFP
0.0309
<0.0001
x6 x3
P F2 F4
g
Adult recombination
(3x 60mg/kg tamoxifen dose)
Frequency (%)
x2 x4 x4 x5 x10 x3 x3
CD31/45- CD31+ CD45+
Lung
Kidney
Liver
Hepatoc.
Heart
Cardiom.
Brain
BoneMarrow
LSK+
MP
DAPI MbTomato MbYFP
Liver
Heart
Rosa26 - CAG-FlpoERT2
Tg-CAG-FlpOERT2 (F2)
Tg-CAG-FlpOERT2 (F4)
iFlpMTomato-Cre / MYFP
h
CRISPR/Cas9 to generate Tg(Cdh5(PAC)-FlpoERT2)
Cas9
gRNA
Cdh5 gRNA
Multicopy
Cdh5 Cre ERT2
Cdh5 FlpO ERT2
Donor
2 Founders
P F1 F2
Cdh5-CreERT2
Cdh5-FlpOERT2
i
Copy number
x1 x1 x4 <1 x4 x1 x3
Cre Ctrl.
FlpO Ctrl.
Cdh5-CreERT2
Founder1 (Cre)
Founder 1 (FlpO)
Founder 2 (Cre)
Founder 2 (FlpO)
j
Cdh5-FlpOERT2 Founder 1
iFlpMTomato-Cre / MYFP
Recombination frequency (%)
E12.5 embryos
Post Natal retina
Adult Lung
Adult Liver
Adult Heart
Adult Kidney
Adult Aorta
Embryo
Postnatal Retina
Adult Heart
ERG MbTomato MbYFP

Figure 3

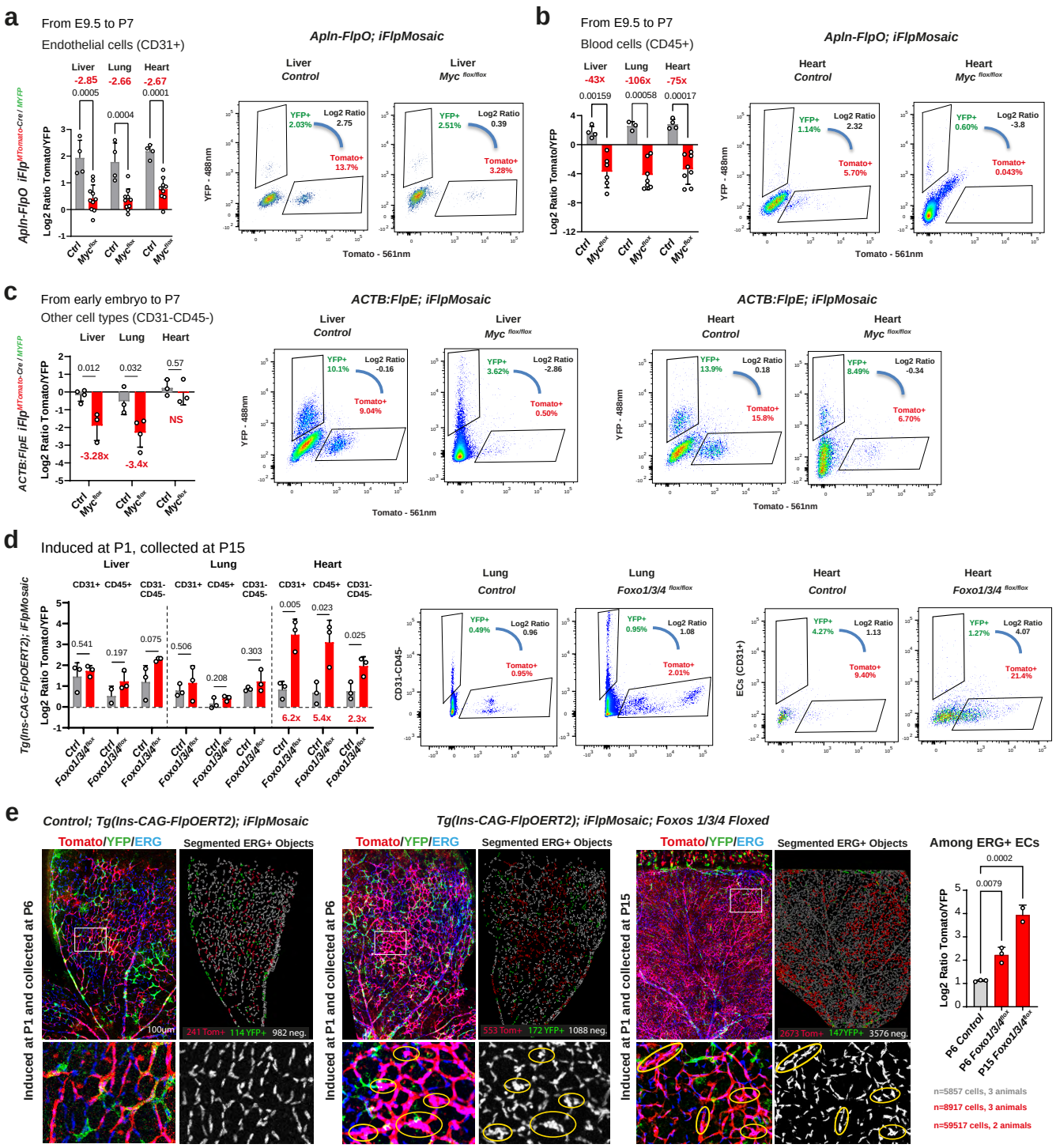
a
From E9.5 to P7
Endothelial cells (CD31+)
Apln-FlpO; iFlpMosaic
Liver
Lung
Heart
Log2 Ratio Tomato/YFP
Control
Myc flox/flox
YFP+
Tomato+
Log2 Ratio
YFP - 488nm
Tomato - 561nm
b
From E9.5 to P7
Blood cells (CD45+)
Apln-FlpO; iFlpMosaic
c
From early embryo to P7
Other cell types (CD31-CD45-)
ACTB:FlpE; iFlpMosaic
NS
d
Induced at P1, collected at P15
CD31+
CD45+
CD31-CD45-
Foxo1/3/4 flox/flox
ECs (CD31+)
e
Control; Tg(Ins-CAG-FlpOERT2); iFlpMosaic
Tg(Ins-CAG-FlpOERT2); iFlpMosaic; Foxos 1/3/4 Floxed
Tomato/YFP/ERG
Segmented ERG+ Objects
Among ERG+ ECs
Induced at P1 and collected at P6
Induced at P1 and collected at P15
100µm
n=5857 cells, 3 animals
n=8917 cells, 3 animals
n=59517 cells, 2 animals

Figure 4

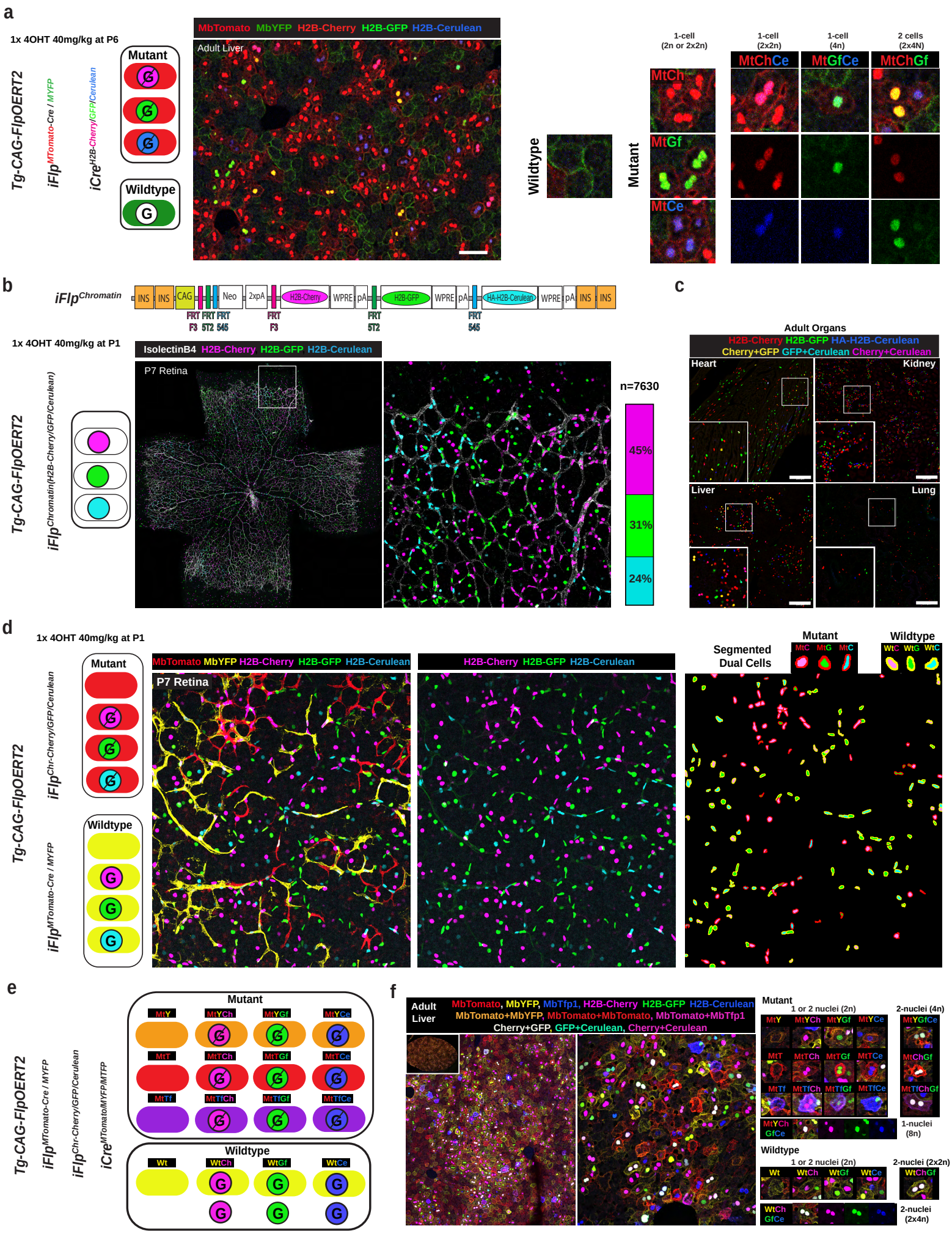
a
1x 4OHT 40mg/kg at P6
Tg-CAG-FlpOERT2
iFlp MTomato-Cre / MYFP
iCre H2B-Cherry/GFP/Cerulean
Mutant
Wildtype
MbTomato MbYFP H2B-Cherry H2B-GFP H2B-Cerulean
Adult Liver
Wildtype
Mutant
1-cell (2n or 2x2n)
1-cell (2x2n)
1-cell (4n)
2 cells (2x4N)
MtCh
MtGf
MtCe
MtChCe
MtGfCe
MtChGf
b
iFlp Chromatin
INS INS CAG Neo 2xpA H2B-Cherry WPRE pA H2B-GFP WPRE pA HA-H2B-Cerulean WPRE pA INS INS
FRT FRT FRT
F3 5T2 545
FRT
F3
FRT
5T2
FRT
545
1x 4OHT 40mg/kg at P1
Tg-CAG-FlpOERT2
iFlp Chromatin(H2B-Cherry/GFP/Cerulean)
IsolectinB4 H2B-Cherry H2B-GFP H2B-Cerulean
P7 Retina
n=7630
45%
31%
24%
c
Adult Organs
H2B-Cherry H2B-GFP HA-H2B-Cerulean
Cherry+GFP GFP+Cerulean Cherry+Cerulean
Heart
Kidney
Liver
Lung
d
1x 4OHT 40mg/kg at P1
Tg-CAG-FlpOERT2
iFlp Chr-Cherry/GFP/Cerulean
iFlp MTomato-Cre / MYFP
Mutant
Wildtype
MbTomato MbYFP H2B-Cherry H2B-GFP H2B-Cerulean
P7 Retina
H2B-Cherry H2B-GFP H2B-Cerulean
Segmented Dual Cells
Mutant
Wildtype
MtC MtG MtC
WtC WtG WtC
e
Tg-CAG-FlpOERT2
iFlp MTomato-Cre / MYFP
iFlp Chr-Cherry/GFP/Cerulean
iCre MTomato/MYFP/MTFP
Mutant
MtY MtYCh MtYGf MtYCe
MtT MtTCh MtTGf MtTCe
MtTf MtTfCh MtTfGf MtTfCe
Wildtype
Wt WtCh WtGf WtCe
f
Adult Liver
MbTomato, MbYFP, MbTfp1, H2B-Cherry H2B-GFP H2B-Cerulean
MbTomato+MbYFP, MbTomato+MbTomato, MbTomato+MbTfp1
Cherry+GFP, GFP+Cerulean, Cherry+Cerulean
Mutant
1 or 2 nuclei (2n)
2-nuclei (4n)
MtY MtYCh MtYGf MtYCe
MtT MtTCh MtTGf MtTCe
MtTf MtTfCh MtTfGf MtTfCe
MtYGfCe
MtChGf
MtTfChGf
MtYCh GfCe
1-nuclei (8n)
Wildtype
1 or 2 nuclei (2n)
2-nuclei (2x2n)
Wt WtCh WtGf WtCe
WtChGf
WtCh GfCe
2-nuclei (2x4n)

Figure 5

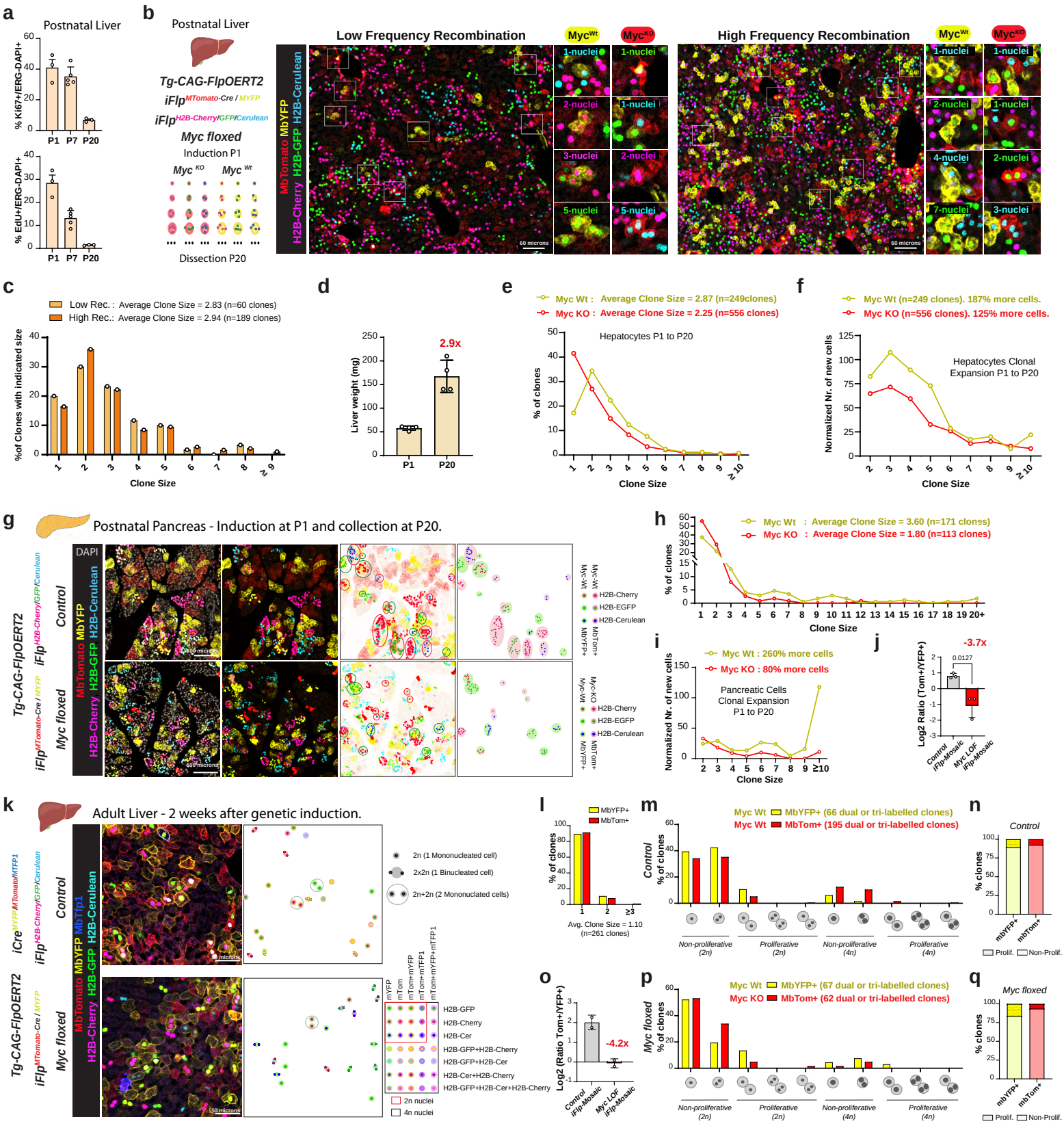
a
Postnatal Liver
% Ki67+/ERG-DAPI+
% EdU+/ERG-DAPI+
P1 P7 P20
b
Postnatal Liver
Tg-CAG-FlpOERT2
iFlp MTomato-Cre / MYFP
iFlp H2B-Cherry/GFP/Cerulean
Myc floxed
Induction P1
Myc KO Myc Wt
Dissection P20
Low Frequency Recombination
High Frequency Recombination
MbTomato MbYFP
H2B-Cherry H2B-GFP H2B-Cerulean
1-nuclei
2-nuclei
3-nuclei
4-nuclei
5-nuclei
7-nuclei
60 microns
c
Low Rec. : Average Clone Size = 2.83 (n=60 clones)
High Rec.: Average Clone Size = 2.94 (n=189 clones)
%of Clones with indicated size
Clone Size
d
2.9x
Liver weight (mg)
P1 P20
e
Myc Wt : Average Clone Size = 2.87 (n=249clones)
Myc KO : Average Clone Size = 2.25 (n=556 clones)
Hepatocytes P1 to P20
% of clones
Clone Size
f
Myc Wt (n=249 clones). 187% more cells.
Myc KO (n=556 clones). 125% more cells.
Hepatocytes Clonal Expansion P1 to P20
Normalized Nr. of new cells
Clone Size
g
Postnatal Pancreas - Induction at P1 and collection at P20.
Tg-CAG-FlpOERT2
iFlp MTomato-Cre / MYFP
iFlp H2B-Cherry/GFP/Cerulean
Control
Myc floxed
DAPI
MbTomato MbYFP
H2B-Cherry H2B-GFP H2B-Cerulean
400 microns
Myc-Wt
Myc-KO
MbYFP+
MbTom+
H2B-Cherry
H2B-EGFP
H2B-Cerulean
h
Myc Wt : Average Clone Size = 3.60 (n=171 clones)
Myc KO : Average Clone Size = 1.80 (n=113 clones)
% of clones
Clone Size
i
Myc Wt : 260% more cells
Myc KO : 80% more cells
Pancreatic Cells Clonal Expansion P1 to P20
Normalized Nr. of new cells
Clone Size
j
-3.7x
0.0127
Log2 Ratio (Tom+/YFP+)
Control iFlp-Mosaic
Myc LOF iFlp-Mosaic
k
Adult Liver - 2 weeks after genetic induction.
iCre MYFP-MTomato/MTFP1
iFlp H2B-Cherry/GFP/Cerulean
Control
Tg-CAG-FlpOERT2
iFlp MTomato-Cre / MYFP
Myc floxed
MbTomato MbYFP MbTfp1
H2B-Cherry H2B-GFP H2B-Cerulean
50 microns
2n (1 Mononucleated cell)
2x2n (1 Binucleated cell)
2n+2n (2 Mononuclated cells)
mYFP
mTom
mTom+mYFP
mTom+mTFP1
mTom+mYFP+mTFP1
H2B-GFP
H2B-Cherry
H2B-Cer
H2B-GFP+H2B-Cherry
H2B-GFP+H2B-Cer
H2B-Cer+H2B-Cherry
H2B-GFP+H2B-Cer+H2B-Cherry
2n nuclei
4n nuclei
l
MbYFP+
MbTom+
% of clones
Avg. Clone Size = 1.10 (n=261 clones)
m
Myc Wt MbYFP+ (66 dual or tri-labelled clones)
Myc Wt MbTom+ (195 dual or tri-labelled clones)
Control
% of clones
Non-proliferative (2n)
Proliferative (2n)
Non-proliferative (4n)
Proliferative (4n)
n
Control
% clones
mbYFP+
mbTom+
Prolif.
Non-Prolif.
o
-4.2x
Log2 (Ratio Tom+/YFP+)
Control iFlp-Mosaic
Myc LOF iFlp-Mosaic
p
Myc Wt MbYFP+ (67 dual or tri-labelled clones)
Myc KO MbTom+ (62 dual or tri-labelled clones)
Myc floxed
% of clones
Non-proliferative (2n)
Proliferative (2n)
Non-proliferative (4n)
Proliferative (4n)
q
Myc floxed
% clones
mbYFP+
mbTom+
Prolif.
Non-Prolif.

Figure 6

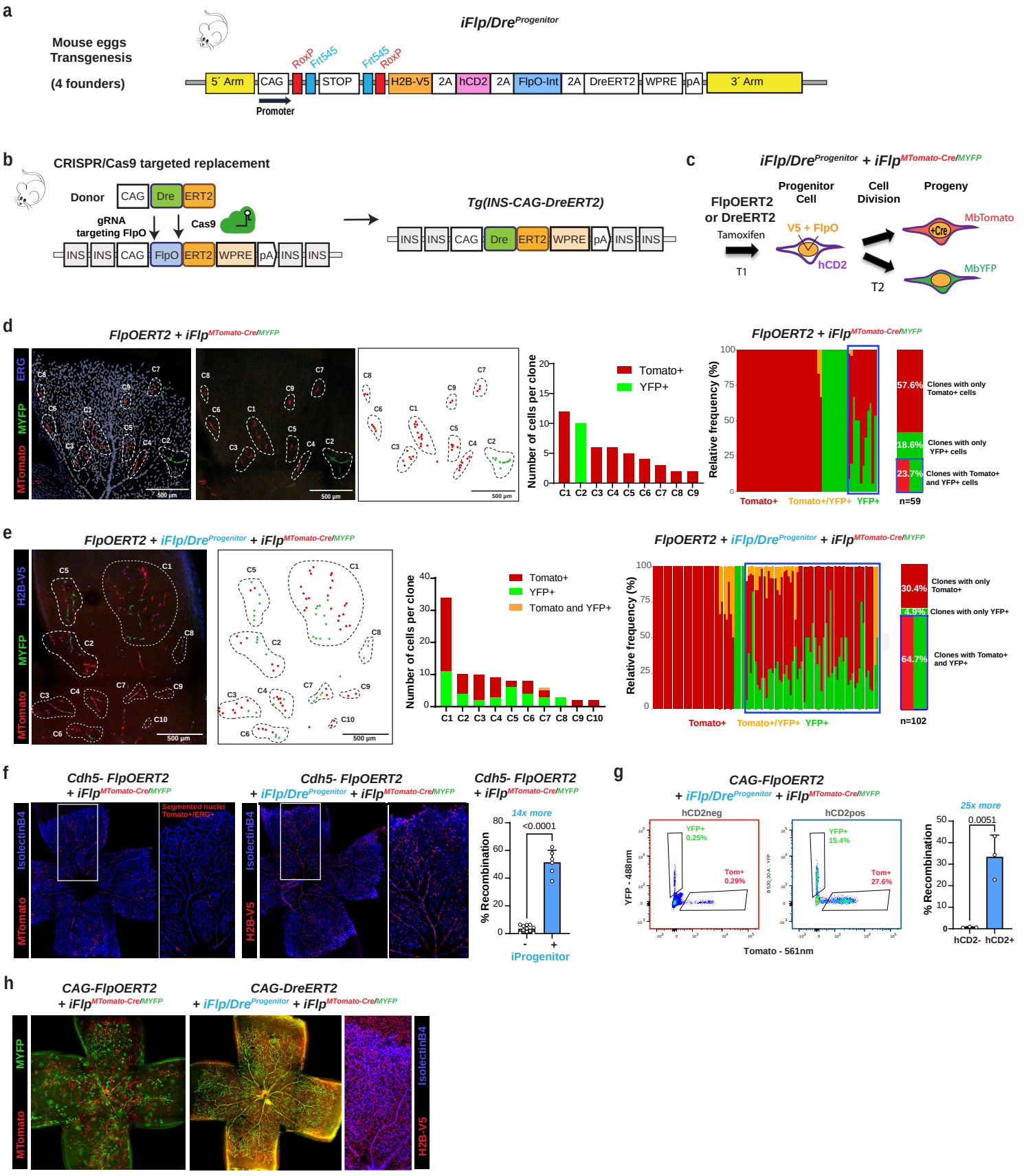
a
Mouse eggs
Transgenesis
(4 founders)
iFlp/Dre Progenitor
RoxP
Frt545
Frt545
RoxP
5´ Arm
CAG
STOP
H2B-V5
2A
hCD2
2A
FlpO-Int
2A
DreERT2
WPRE
pA
3´ Arm
Promoter
b
CRISPR/Cas9 targeted replacement
Donor
CAG
Dre
ERT2
gRNA
targeting FlpO
Cas9
INS
INS
CAG
FlpO
ERT2
WPRE
pA
INS
INS
Tg(INS-CAG-DreERT2)
INS
INS
CAG
Dre
ERT2
WPRE
pA
INS
INS
c
iFlp/Dre Progenitor + iFlp MTomato-Cre/MYFP
FlpOERT2
or DreERT2
Tamoxifen
T1
Progenitor
Cell
V5 + FlpO
hCD2
Cell
Division
T2
Progeny
+Cre
MbTomato
MbYFP
d
FlpOERT2 + iFlp MTomato-Cre/MYFP
ERG
MYFP
MTomato
500 µm
Number of cells per clone
Tomato+
YFP+
C1 C2 C3 C4 C5 C6 C7 C8 C9
Relative frequency (%)
Tomato+
Tomato+/YFP+
YFP+
57.6%
Clones with only Tomato+ cells
18.6%
Clones with only YFP+ cells
23.7%
Clones with Tomato+ and YFP+ cells
n=59
e
FlpOERT2 + iFlp/Dre Progenitor + iFlp MTomato-Cre/MYFP
H2B-V5
MYFP
MTomato
500 µm
Number of cells per clone
Tomato+
YFP+
Tomato and YFP+
C1 C2 C3 C4 C5 C6 C7 C8 C9 C10
Relative frequency (%)
Tomato+
Tomato+/YFP+
YFP+
30.4%
Clones with only Tomato+
4.9%
Clones with only YFP+
64.7%
Clones with Tomato+ and YFP+
n=102
f
Cdh5- FlpOERT2
+ iFlp MTomato-Cre/MYFP
IsolectinB4
MTomato
Segmented nuclei
Tomato+/ERG+
Cdh5- FlpOERT2
+ iFlp/Dre Progenitor + iFlp MTomato-Cre/MYFP
IsolectinB4
H2B-V5
Cdh5- FlpOERT2
+ iFlp MTomato-Cre/MYFP
14x more
<0.0001
% Recombination
-
+
iProgenitor
g
CAG-FlpOERT2
+ iFlp/Dre Progenitor + iFlp MTomato-Cre/MYFP
hCD2neg
hCD2pos
YFP+
0.25%
Tom+
0.29%
YFP+
15.4%
Tom+
27.6%
YFP - 488nm
Tomato - 561nm
25x more
0.0051
% Recombination
hCD2-
hCD2+
h
CAG-FlpOERT2
+ iFlp MTomato-Cre/MYFP
CAG-DreERT2
+ iFlp/Dre Progenitor + iFlp MTomato-Cre/MYFP
MYFP
MTomato
IsolectinB4
H2B-V5

Figure 7

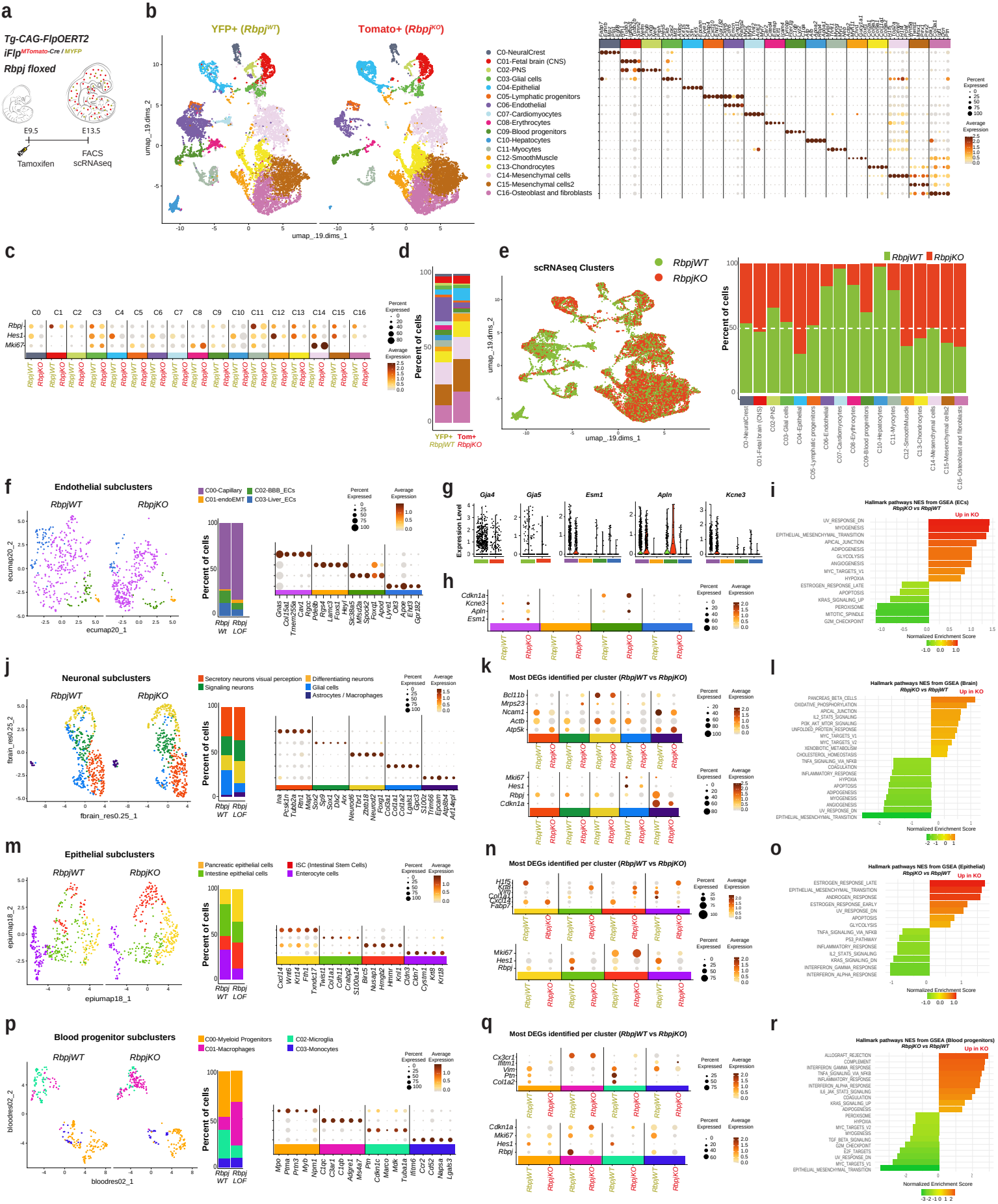
a
Tg-CAG-FlpOERT2
iFlp MTomato-Cre / MYFP
Rbpj floxed
E9.5
E13.5
Tamoxifen
FACS
scRNAseq
b
YFP+ (RbpjWT)
Tomato+ (RbpjKO)
umap_.19.dims_2
umap_.19.dims_1
C0-NeuralCrest
C01-Fetal brain (CNS)
C02-PNS
C03-Glial cells
C04-Epithelial
C05-Lymphatic progenitors
C06-Endothelial
C07-Cardiomyocytes
C08-Erythrocytes
C09-Blood progenitors
C10-Hepatocytes
C11-Myocytes
C12-SmoothMuscle
C13-Chondrocytes
C14-Mesenchymal cells
C15-Mesenchymal cells2
C16-Osteoblast and fibroblasts
Percent Expressed
Average Expression
c
Rbpj
Hes1
Mki67
d
Percent of cells
YFP+ RbpjWT
Tom+ RbpjKO
e
scRNAseq Clusters
RbpjWT
RbpjKO
umap_.19.dims_2
umap_.19.dims_1
Percent of cells
f
Endothelial subclusters
RbpjWT
RbpjKO
ecumap20_2
ecumap20_1
C00-Capillary
C01-endoEMT
C02-BBB_ECs
C03-Liver_ECs
Percent of cells
Rbpj Wt
Rbpj LOF
g
Gja4
Gja5
Esm1
Apln
Kcne3
Expression Level
h
Cdkn1a
Kcne3
Apln
Esm1
i
Hallmark pathways NES from GSEA (ECs)
RbpjKO vs RbpjWT
Up in KO
UV_RESPONSE_DN
MYOGENESIS
EPITHELIAL_MESENCHYMAL_TRANSITION
APICAL_JUNCTION
ADIPOGENESIS
GLYCOLYSIS
ANGIOGENESIS
MYC_TARGETS_V1
HYPOXIA
ESTROGEN_RESPONSE_LATE
APOPTOSIS
KRAS_SIGNALING_UP
PEROXISOME
MITOTIC_SPINDLE
G2M_CHECKPOINT
Normalized Enrichment Score
j
Neuronal subclusters
RbpjWT
RbpjKO
fbrain_res0.25_2
fbrain_res0.25_1
Secretory neurons visual perception
Signaling neurons
Differentiating neurons
Glial cells
Astrocytes / Macrophages
Percent of cells
Rbpj WT
Rbpj LOF
k
Most DEGs identified per cluster (RbpjWT vs RbpjKO)
Bcl11b
Mrps23
Ncam1
Actb
Atp5k
Mki67
Hes1
Rbpj
Cdkn1a
l
Hallmark pathways NES from GSEA (Brain)
RbpjKO vs RbpjWT
Up in KO
PANCREAS_BETA_CELLS
OXIDATIVE_PHOSPHORYLATION
APICAL_JUNCTION
IL2_STAT5_SIGNALING
PI3K_AKT_MTOR_SIGNALING
UNFOLDED_PROTEIN_RESPONSE
MYC_TARGETS_V1
MYC_TARGETS_V2
XENOBIOTIC_METABOLISM
CHOLESTEROL_HOMEOSTASIS
TNFA_SIGNALING_VIA_NFKB
COAGULATION
INFLAMMATORY_RESPONSE
HYPOXIA
APOPTOSIS
ADIPOGENESIS
MYOGENESIS
ANGIOGENESIS
UV_RESPONSE_DN
EPITHELIAL_MESENCHYMAL_TRANSITION
Normalized Enrichment Score
m
Epithelial subclusters
RbpjWT
RbpjKO
epiumap18_2
epiumap18_1
Pancreatic epithelial cells
Intestine epithelial cells
ISC (Intestinal Stem Cells)
Enterocyte cells
Percent of cells
Rbpj WT
Rbpj LOF
n
Most DEGs identified per cluster (RbpjWT vs RbpjKO)
Mki67
Hes1
Rbpj
o
Hallmark pathways NES from GSEA (Epithelial)
RbpjKO vs RbpjWT
Up in KO
ESTROGEN_RESPONSE_LATE
EPITHELIAL_MESENCHYMAL_TRANSITION
ANDROGEN_RESPONSE
ESTROGEN_RESPONSE_EARLY
UV_RESPONSE_DN
APOPTOSIS
GLYCOLYSIS
TNFA_SIGNALING_VIA_NFKB
P53_PATHWAY
INFLAMMATORY_RESPONSE
IL2_STAT5_SIGNALING
KRAS_SIGNALING_DN
INTERFERON_GAMMA_RESPONSE
INTERFERON_ALPHA_RESPONSE
Normalized Enrichment Score
p
Blood progenitor subclusters
RbpjWT
RbpjKO
bloodres02_2
bloodres02_1
C00-Myeloid Progenitors
C01-Macrophages
C02-Microglia
C03-Monocytes
Percent of cells
Rbpj WT
Rbpj LOF
q
Most DEGs identified per cluster (RbpjWT vs RbpjKO)
Cx3cr1
Ifitm1
Vim
Ptn
Col1a2
Cdkn1a
Mki67
Hes1
Rbpj
r
Hallmark pathways NES from GSEA (Blood progenitors)
RbpjKO vs RbpjWT
Up in KO
ALLOGRAFT_REJECTION
COMPLEMENT
INTERFERON_GAMMA_RESPONSE
TNFA_SIGNALING_VIA_NFKB
INFLAMMATORY_RESPONSE
INTERFERON_ALPHA_RESPONSE
IL6_JAK_STAT3_SIGNALING
COAGULATION
KRAS_SIGNALING_UP
ADIPOGENESIS
PEROXISOME
HYPOXIA
MYC_TARGETS_V2
MYOGENESIS
TGF_BETA_SIGNALING
G2M_CHECKPOINT
E2F_TARGETS
UV_RESPONSE_DN
MYC_TARGETS_V1
EPITHELIAL_MESENCHYMAL_TRANSITION
Normalized Enrichment Score

Supplementary Fig. 1

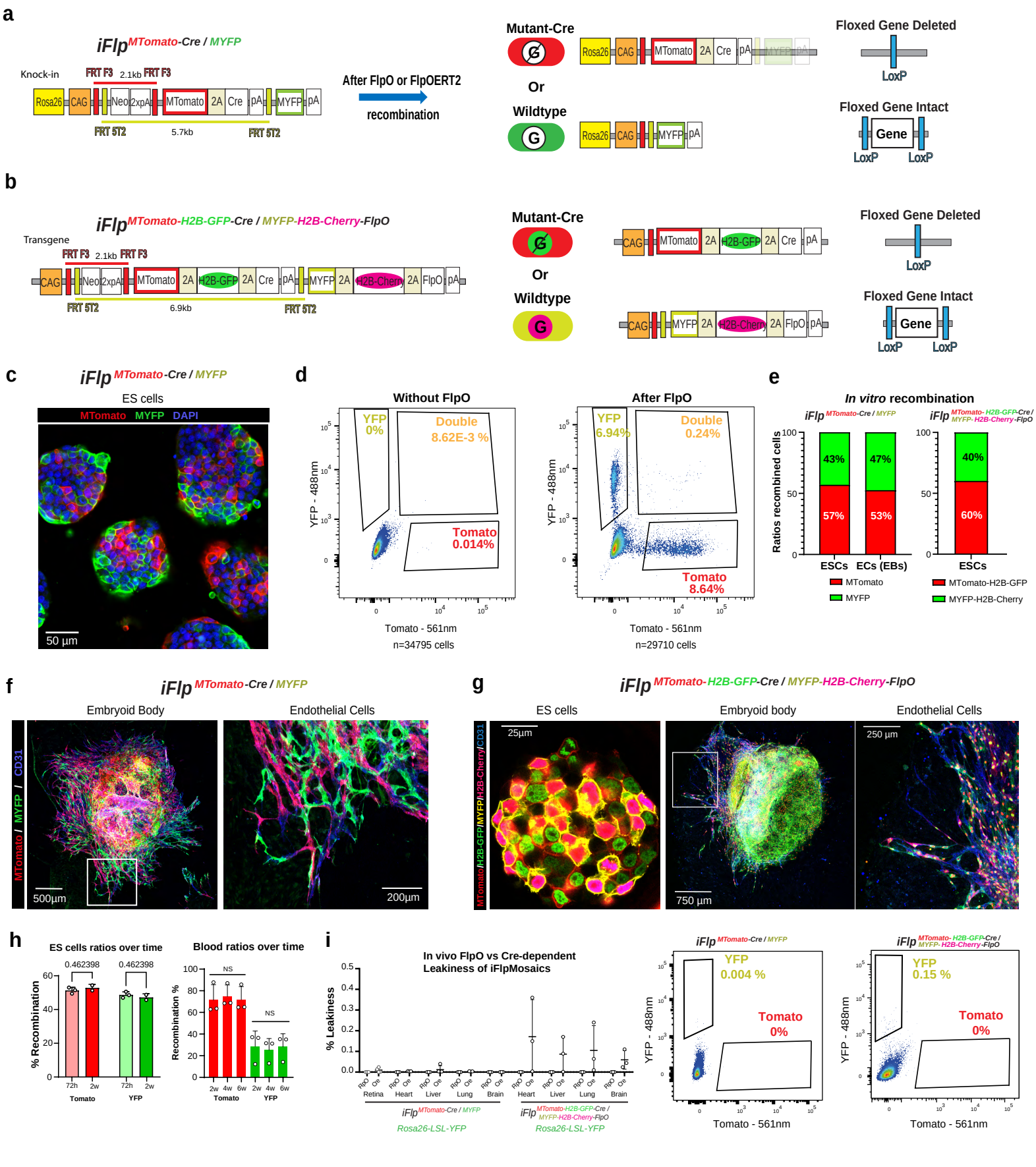

Supplementary Fig. 2

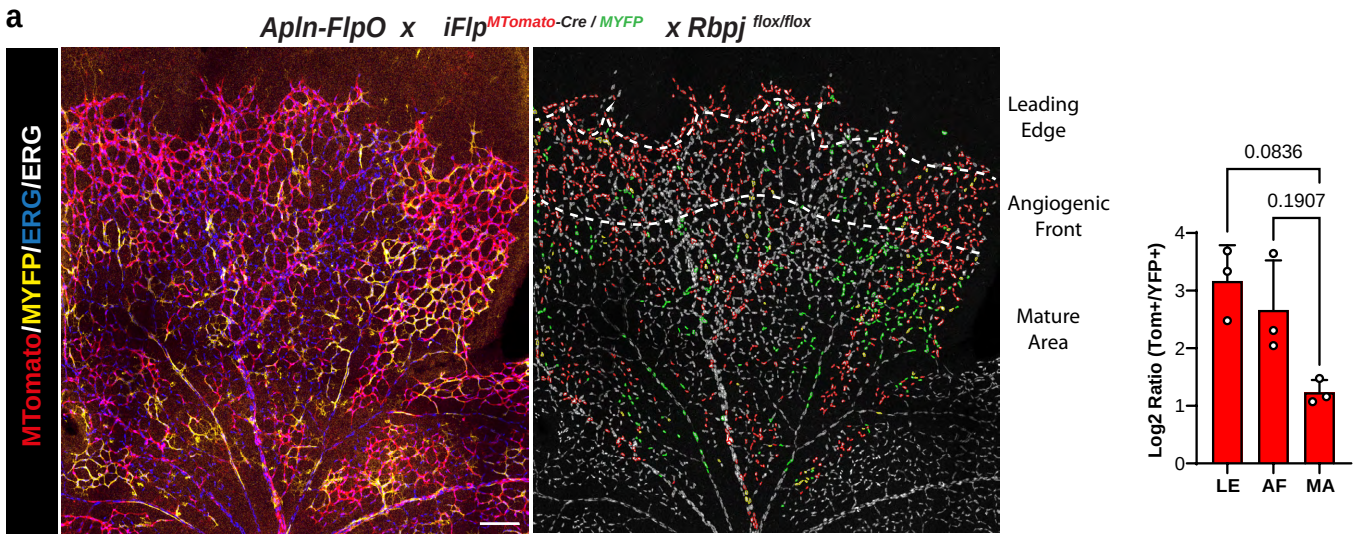

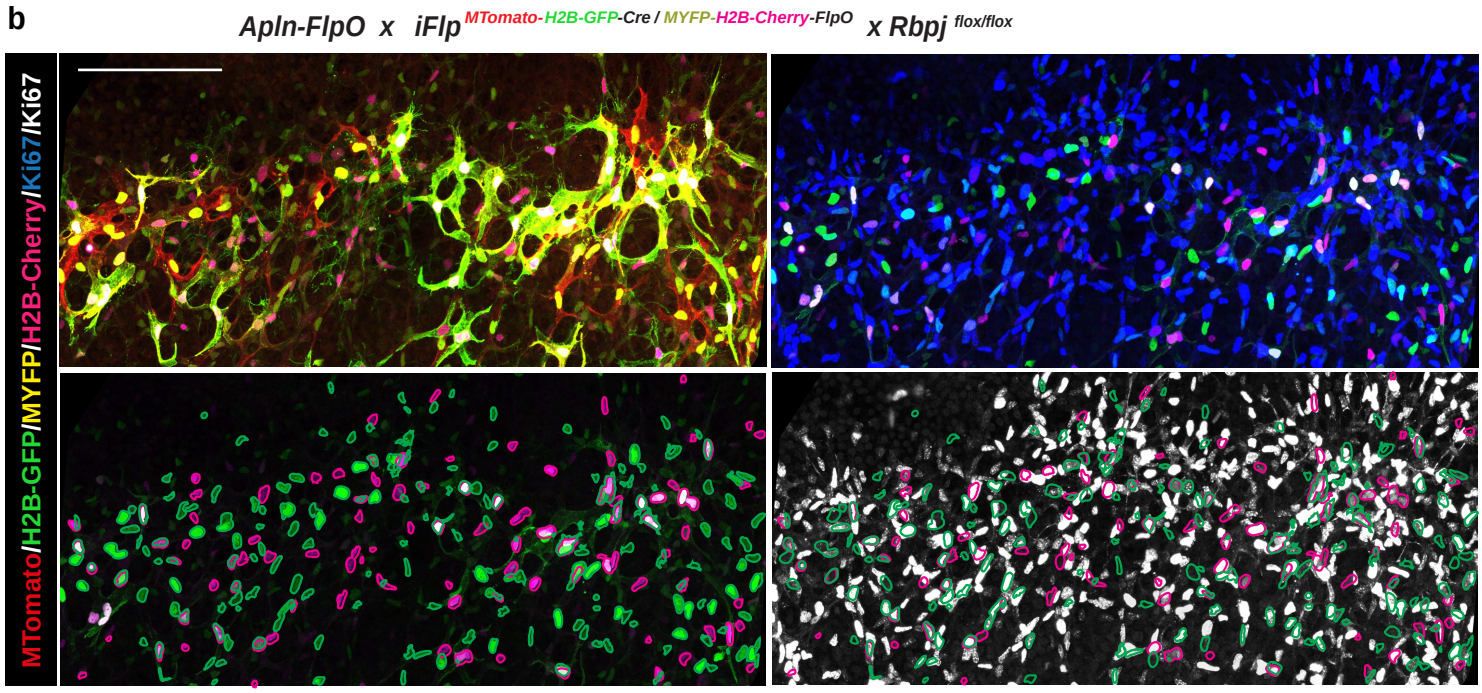

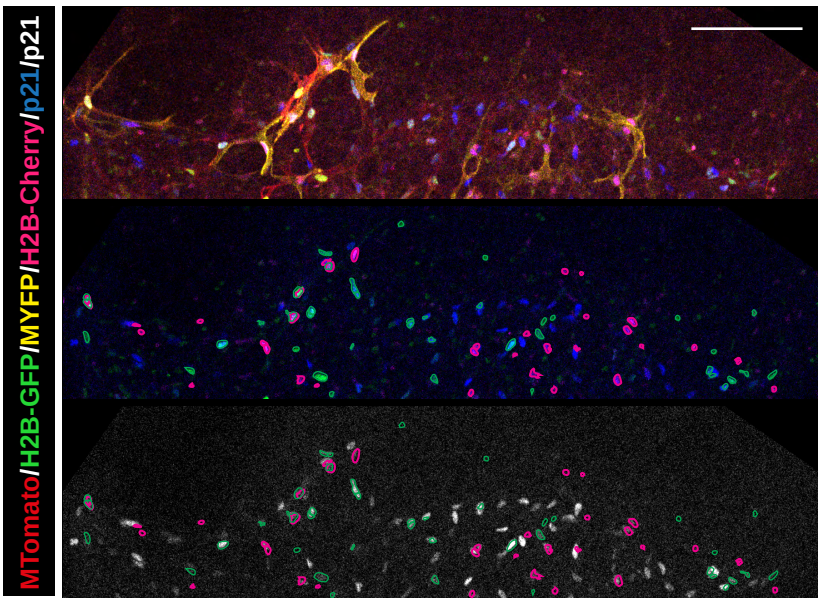

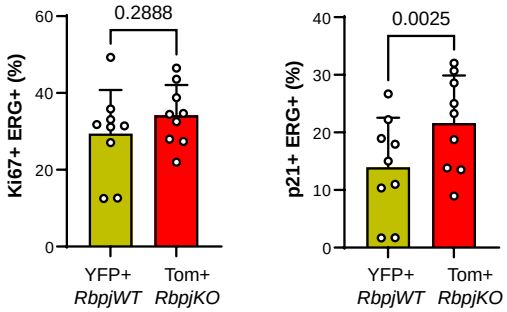

Supplementary Fig. 3

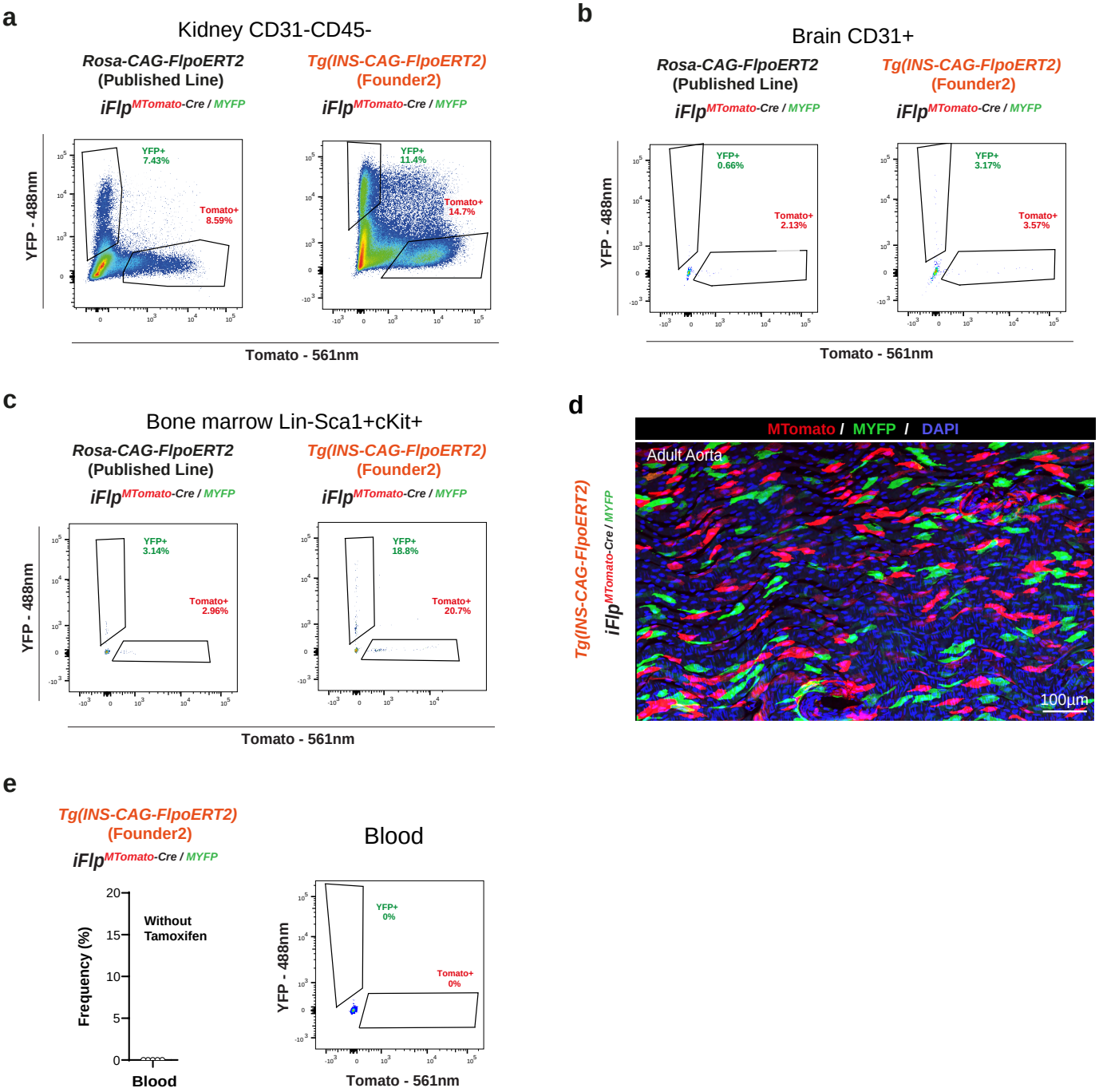

Supplementary Fig. 4

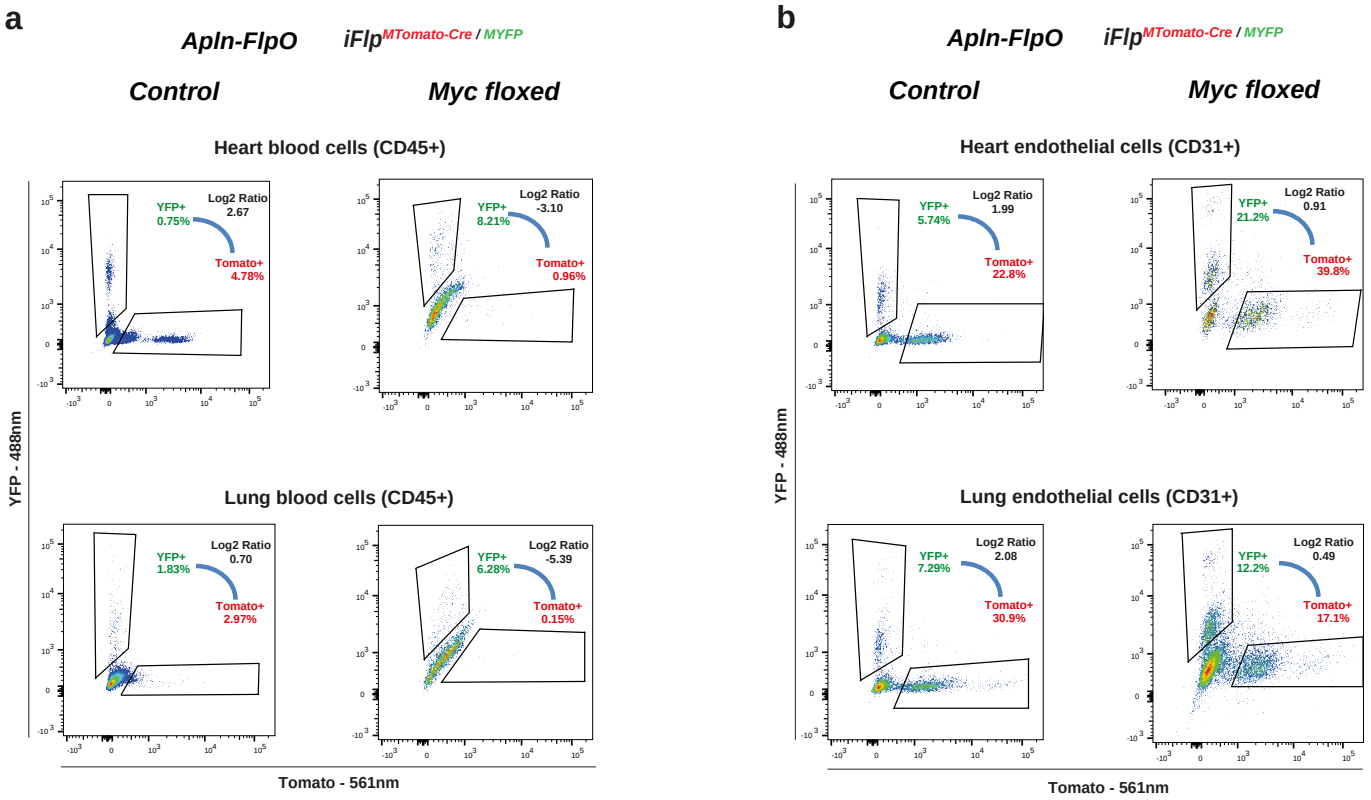

c

iChr2-Mosaic or iCreH2B-Cherry/GFP/Cerulean

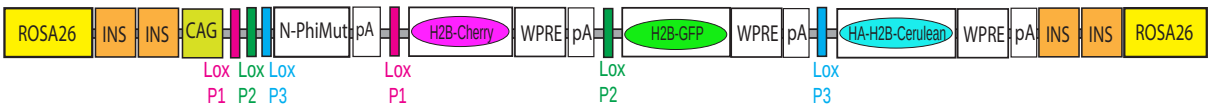

Supplementary Fig. 5

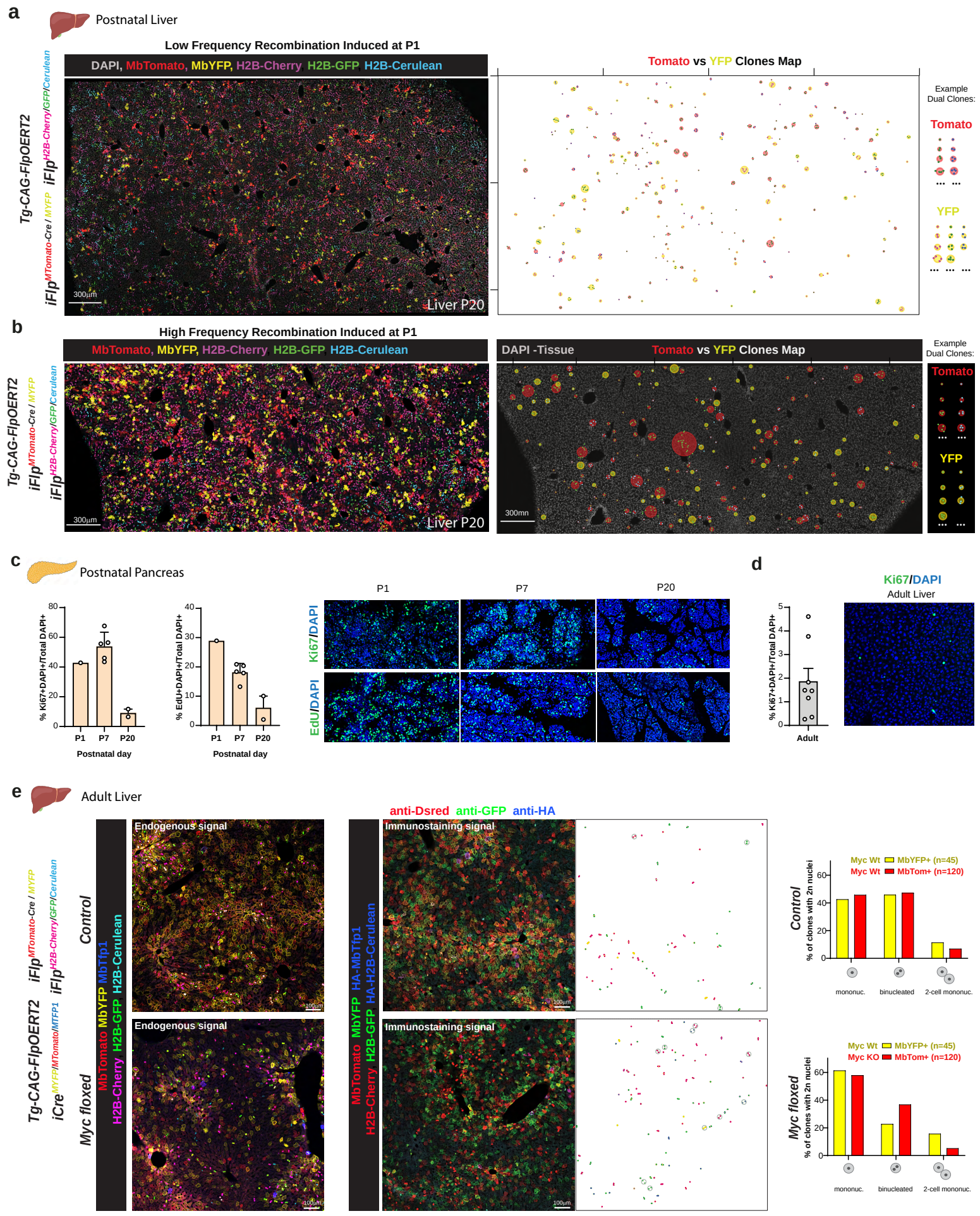

Supplementary Figure 6

a

FlpOERT2 + iFlp/Dre^{Progenitor} + iFlp$^{MTomato\text{-}Cre/MYFP}$

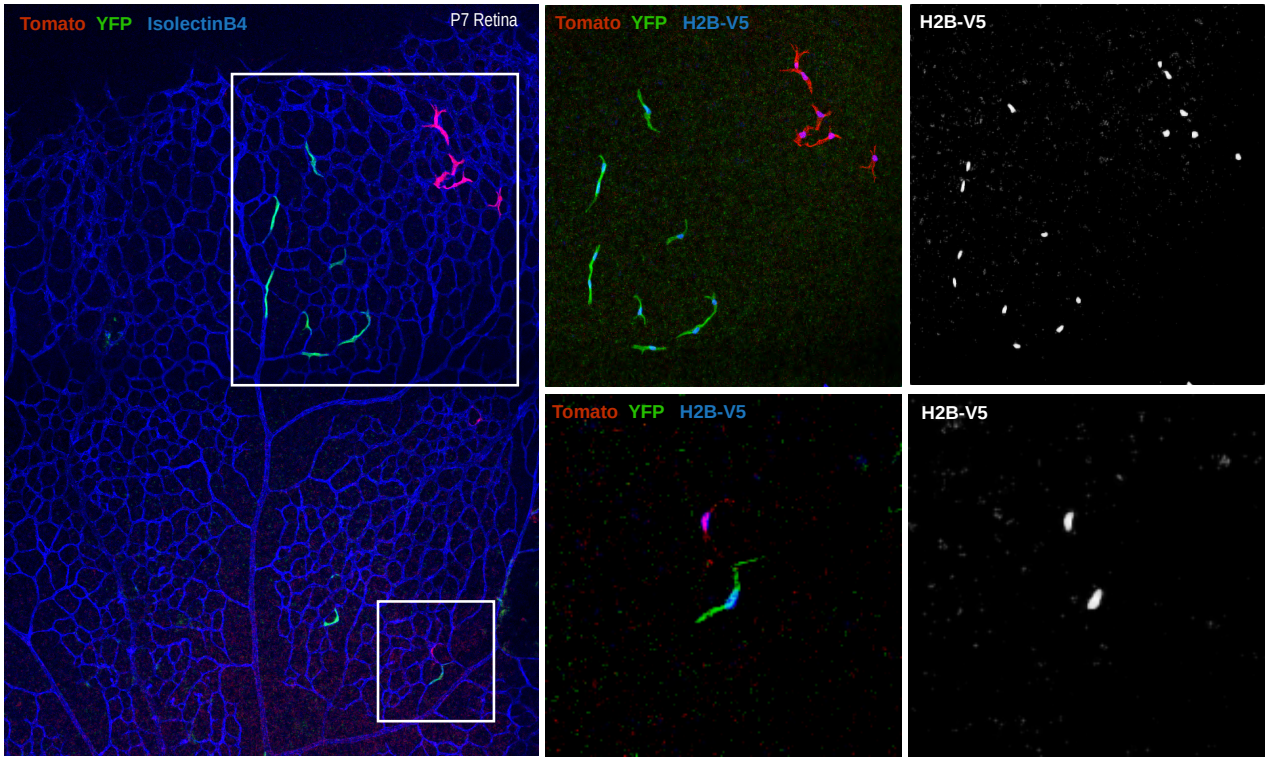

Supplementary Figure 7

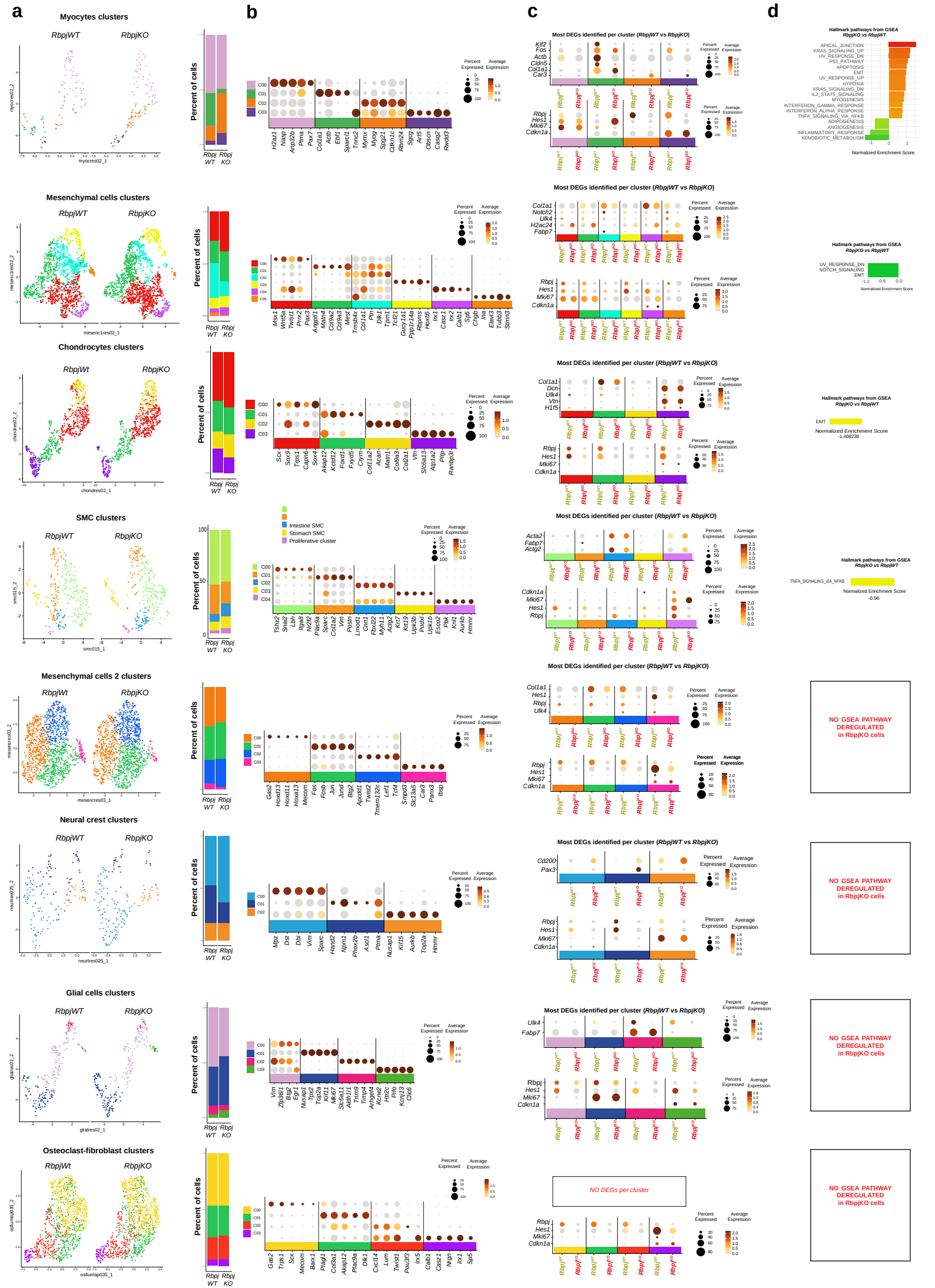

Supplementary Table 1

Ref		Mouse line	Band size	Genotyping primers
Generated in this study	iFlp-Mosaics	*Gt(ROSA)26Sor-iFlpMbTomato-2A-cre/MbYFP*	WT: 250bp KI: 380bp	QPCR MAN YFP F II CTGCCCGACAACCACTACCT RR713 CTTTAAGCCTGCCCAGAAGA WPRE REV GTTGCGTCAGCAAACACAGT RR711 GCACTTGCTCTCCCAAAGTC
		Tg(ROSA)26Sor-iFlpMbTomato-2A-H2B-GFP2A-cre/MbYFP2A-H2B-Cherry-2A-Flpo	TG: 369bp	GFP SEQ F: CGACAACCACTACCTGAGCA CREM R: TCCCTGAACATGTCCATCAG
		Tg(ROSA)26Sor-iFlpChromatin	TG: 300bp	FRT1 DUM F TGTTGTTGAAGCTTGAAGTTCCT CHERRY DUM R GCTCGAAAATGTCGTTCACA
	FlpOERT2	*Tg(Cdh5(PAC)-FlpoERT2)*	TG: 538bp	CDH5 TRANS F: GGAGGCTGGAAAGTAGAGCA FLPO TRANS AND SEQ REV: GTCTTGCACAGGATGTCGAA
		Tg(INS-CAG-FlpoERT2)	TG: 530bp	FLPOERT2 F GENOTYPING GCCCTGGTGTCCAGGTACTA FLPOERT2 R GENOTYPING AGGATCTCTAGCCAGGCACA
	DreERT2	*Tg(INS-CAG-DreERT2)*	TG: 249bp	CAG F: GCAACGTGCTGGTTATTGTG Dre R II: CTAGCGTGGCACCATCTAGC
	FlpO and dre Inducible	*Tg(iFlp/Dre ^{iProgenitor})*	TG: 412bp	AR124 1A HCD2 SEQ: TGAATGGAACTGACCCCGAA NCOI-FLPO R: GTCTTGCACAGGATGTCGAA
Ref		**Mouse line**	**Band size**	**Genotyping primers**
(Lao, Raju, Bai, & Joyner, 2012)	FlpO drivers	*Gt(ROSA)26SorCAG-FlpoERT2*	WT:630bp KI: 309bp	FLPO/ERT2 MUT TTA TGT AAC GCG GAA CTC CA FLPO/ERT2 COM AAA GTC GCT CTG AGT TGT TAT FLPO/ERT2 WT GGA GCG GGA GAA ATG GAT ATG
(Luo et al, 2021)		*Apln-Flpo*	KI: 292bp	HA F CATGGCGTATCCATATGACG FLPO REV GTTCACGATGTCGAAGCTCA
(Farley et al., 2000)		*Gt(ROSA)26Sortm1(FLP1)*	KI: 260bp	FLPES CTAATGTTGTGGGAAATTGGAGC FLPEAS
(de Alboran et al, 2001),	Floxed	*Myc ^{flox}*	WT:315BP MUT: 370BP	MYC FLOX RB F GACAGGGATGTGACCGATTC MYC FLOX RB R GCTCAGTCTCCGGCTATCAC
Paik et al., 2007		*Foxos1 ^{flox}*	FLOX 149 BP WT: 115	FOXO 1 PRIMER A: GCTTAGAGCAGAGATGTTCTCACATT FOXO 1 PRIMER B: CCAGAGTCTTTGTATCAGGCAAATAA FOXO 1 PRIMER D: CAAGTCCATTAATTCAGCACATTGA
Paik et al., 2007		*Foxos3 ^{flox}*	FLOX: 138 WT 100	FOXO 3 PRIMER A: ATTCCTTTGGAAATCAACAAAACT FOXO 3 PRIMER B: TGCTTTGATACTATTCCACAAACCC FOXO 3 PRIMER D: AGATTTATGTTCCCACTTGCTTCCT
Paik et al., 2007		*Foxos4 ^{flox}*	FLOX 555 WT: 343	FOXO 4 PRIMER A: CTTCTCTGTGGGAATAAATGTTTGG FOXO 4 PRIMER B: CTACTTCAAGGACAAGGGTGACAG FOXO 4 PRIMER D: TGAGAAGCCATTGAAGATCAGA
(Han et al, 2002)		*Rbpj ^{flox}*	WT:200bp Flox:350bp	RBPJLOX F ATAATTTGCCAAGCCAAAGC RBPJLOX R GCTCCCCACTGTTGTGAACT
(Srinivas et al, 2001)	Reporter	*Gt(ROSA)26LSL-EYFP*	WT: 250bp KI: 350bp	RR711 GCACTTGCTCTCCCAAAGTC RR713 CTTTAAGCCTGCCCAGAAGA CAG PCR F CGGGGTCATTAGTTCATAGCC CAG PCR R CACCTCGACCATGGTAATAGC
(Madisen et al, 2010)		*Gt(ROSA)26LSL-tdTomato*		
(Pontes-Quero et al., 2017)		*Tg(Rosa)26Sor(iMb2-Control-Mosaic)*	TG: 600bp	LOXP3 SEQ F: TCAATGTATCTTAAGGCGTGACT MTFP1 R: TACTTGGTGAAGGCCCTGTT
		Gt(Rosa)26Sortm1(iChr-Control-Mosaic)	TG: 550bp	CTP PHI F ACGTGAAGCTGAGCAAGGAT CTP H2B R CTTAGTCACCGCCTTCTTGG
(Wang et al, 2010),	Cre drivers	*Tg(Cdh5-CreERT2)*	TG: 600bp	CDH5 TRANS F GGAGGCTGGAAAGTAGAGCA CREM R TCCCTGAACATGTCCATCAG
(Fernandez-Chacon et al, 2019)		*Tg(iSuRe-Cre)*	TG: 350bp	CREM R QPCR MAN MTOMATO F II CCGCTACCTGGTGGAGTTCA

Supplementary Table 2

Antibody	Dilution	Source	Reference
Primary Antibodies			
Biotinilated Isolectin B4	1:100 (IF)	VECTOR LABS	B-1205
Rat anti- mouse p21 Rat monoclonal Clone: HUGO291 Supernatant	1:50 (IF)	CNIO	#
Monoclonal Rabbit anti-ERG [EPR3863]	1:500 (IF)	ABCAM	Ab110639
Goat Polyclonal Anti-GFP and YFP/CFP variants	1:200 (IF)	Acris	R1091P
Anti-PECAM-1 Antibody, clone 2H8 hamster anti mouse CD31	1:200 (IF)	Merck	MAB1398Z
Rabbit anti- DsRed (Living colors)	1:200 (IF)	Clontech	632496
Rabbit anti-RFP/Dsred/Tomato/Cherry CF543 conjugated (Polyclonal)	1:200 (IF)	Biotium	20476
Mouse anti HA-Tag (6E2) Mouse mAb (Alexa Fluor® 647 Conjugate)	1:200 (IF)	Cell Signaling	3444
RABBIT ANTI-RFP/Dsred ConjugatedCF594	1:200 (IF & FC)	Sigma or Biotium	BTIU20422
Rabbit Anti-ERG Alexa Fluor® 647 EPR3864	1:500 (IF)	ABCAM	ab196149
Rat anti-Ki-67 Monoclonal Antibody (SolA15), eFluor 660, eBioscience™	1:250 (IF)	Thermo Fisher Scientific	50-5698-82
APC Rat Anti-Mouse CD31	1:250 (FC)	BD Bioscience	551262
APC-Cyanine7 Rat Anti-Mouse CD45.2	1:250 (FC)	TonboBio	25-0454-U025
Mouse anti HA-Tag (6E2) Mouse mAb (Alexa Fluor® 647 Conjugate)	1:250 (IF)	Cell Signaling	3444
BV711 Rat Anti-Mouse CD31 Clone MEC 13.3 (RUO)	1:250 (FC)	BD Biosciences	740680
Rabbit anti GFP Conj. Alexa-488	1:200 (IF & FC)	Invitrogen	A213111
BD Horizon™ BV605 Rat Anti-Mouse CD45	1:200 (FC)	BD Biosciences	563053
Anti-Mouse CD150 (SLAM) Antibody Brilliant Violet 510™	1:300 (FC)	Biolegend	115929
Anti-Mouse CD48 APC Cy7	1:100 (FC)	Biolegend	103432
Anti-Mouse CD117 (c-kit) PercP Cy5.5	1:200 (FC)	Biolegend	105824
Anti-Mouse Ly-6A/E (Sca-1) FITC	1:200 (FC)	eBioscience	11-5981-85
Biotin Mouse Lineage Depletion Cocktail	1:200 (FC)	BD Biosciences	51-9000794
Secondary Antibodies			
Streptavidin, Alexa Fluor® 405 conjugate	1:200 (IF)	Thermo Fisher Scientific	ST32351
Donkey Anti-Rat IgG H&L (Alexa Fluor® 647) preadsorbed	1:400 (IF)	ABCAM	ab150155
Cy™3 AffiniPure Fab Fragment Donkey Anti-Rabbit IgG (H+L)	1:400 (IF)	Jackson	711-167-003
AffiniPure Goat Anti-Armenian Hamster Alexa680	1:400 (IF)	Jackson	127-625-16

Supplementary Table 3

Taqman Assays

Gene Symbol	Dye	Assay ID	Source
Rbpj	FAM-MGB	Mm01217627_g1	Thermo Fisher
Myc	FAM-MGB	Mm00487804_m1	Thermo Fisher
Mycn	FAM-MGB	Mm00476449_m1	Thermo Fisher
Notch1	FAM-MGB	Mm00435245_m1	Thermo Fisher
Pecam1	FAM-MGB	Mm01242584_m1	Thermo Fisher
Gapdh	FAM-MGB	Mm99999915_g1	Thermo Fisher